Preprint Cambridge Centre for Computational Chemical Engineering ISSN 1473 – 4273

Understanding the anatase-rutile stability in flame-made TiO_2

Manoel Y. Manuputty[1,2], Casper S. Lindberg[1,2], Jochen A. H. Dreyer[1,2,3], Jethro Akroyd[1,2], John Edwards[4], Markus Kraft[1,2,5]

released: September 13, 2019

[1] Department of Chemical Engineering
and Biotechnology
University of Cambridge
Philippa Fawcett Drive
Cambridge, CB3 0AS
United Kingdom

E-mail: mk306@cam.ac.uk

[2] CARES
Cambridge Centre for Advanced
Research and Education in Singapore
1 Create Way
CREATE Tower, #05-05
Singapore, 138602

[3] CoaST
Department of Chemical and
Biochemical Engineering
Technical University of Denmark
Building 229
2800 Kgs. Lyngby
Denmark

[4] Venator
Titanium House
Hanzard Drive
Wynyard Park, TS22 5FD
United Kingdom

[5] School of Chemical
and Biomedical Engineering
Nanyang Technological University
62 Nanyang Drive
Singapore, 637459

Preprint No. 238

UNIVERSITY OF CAMBRIDGE

Keywords: anatase, rutile, phase stability, flame synthesis, particle model

Edited by
Computational Modelling Group
Department of Chemical Engineering and Biotechnology
University of Cambridge
Philippa Fawcett Drive
Cambridge CB3 0AS
United Kingdom

E-Mail: c4e@cam.ac.uk
World Wide Web: http://como.ceb.cam.ac.uk/

Abstract

The relative stability of anatase and rutile in stagnation flame synthesis with stoichiometric mixtures is investigated experimentally. The measurements reveal a high sensitivity of anatase-rutile composition to the flame dilution. It is demonstrated that anatase formation is favoured in more dilute (colder) flames while rutile is favoured in less dilute (hotter) flames. A particle model with a detailed description of aggregate morphology and crystal phase composition is applied to investigate the anatase-rutile stability. A size-dependent phase transformation model is implemented in which rutile is formed for particles larger than a "crossover" size while anatase is formed for those smaller. Two formation mechanisms/pathways are discussed and evaluated. In the first pathway, the nascent particles are assumed to be stoichiometric and the crossover size is given by thermodynamic quantities. This hypothesis captures the general trend in the measured anatase-rutile composition but fails to explain the sensitivity. In the second pathway, non-stoichiometric TiO_{2-x} oxide intermediates are assumed and the crossover size is hypothesised to be composition-dependent. This shows an excellent agreement with the experimental data. However, this hypothesis is found to be strongly influenced by assumptions about the initial particle growth stages. This study demonstrates the importance of a better description of the high-temperature chemistry and initial clustering mechanism in order to understand the crystal phase formation.

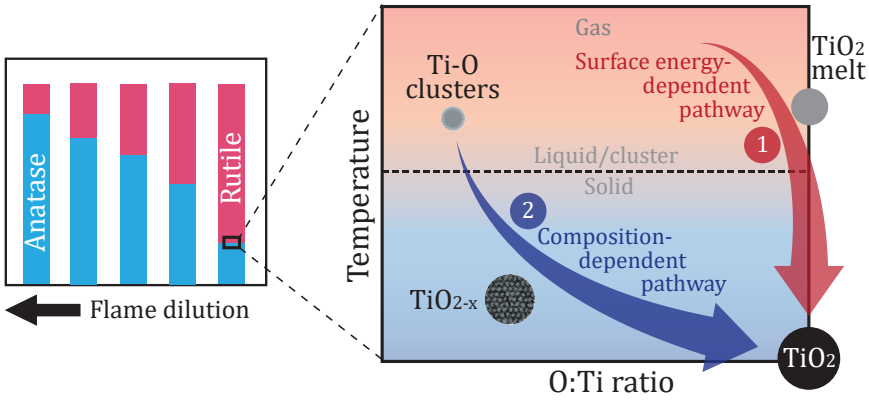

Highlights

- The detailed particle model type space is extended to describe the crystal phase composition.
- Experimental phase quantification is performed for samples prepared with stoichiometric flames.
- Anatase-rutile stability is strongly influenced by the flame dilution with argon.
- Three different models are proposed and evaluated to understand the origin of the sensitivity.

Contents

1 Introduction

Synthesis of TiO_2 particles from gas-phase precurors, i.e."bottom-up" approach, is an industrially important process. Crucial properties of the prepared TiO_2 such as phase composition and particle morphology are strongly influenced by the synthesis conditions. Understanding the phase formation mechanism and particle growth is therefore of great research interest [51].

Thermodynamically, the relative stability of anatase and rutile is mainly governed by the competing contributions of bulk and surface energies. Rutile is the thermodynamically stable phase for bulk TiO_2. However, below a certain particle size, surface energy dominates, leading to anatase nanoparticles being energetically more stable. The appearance of a "crossover" size has been supported by experimental observations [53, 54]. In addition, the size-dependent stability can also be captured by a simple thermodynamic model of melting point depression of nano-sized particles [18] in which the melting point of nanoparticles depends on the solid/liquid interfacial energy.

While the surface energy-dependent model proved satisfactory in some cases [53], it falls short of explaining the effect of other factors which are often observed for bottom-up synthesis, including flame-assisted synthesis. Studies have shown that the phase composition depends on factors such as temperature, oxygen environment, precursor, residence time, etc. It is generally accepted that oxygen-lean environments favour rutile formation over anatase. For flame synthesis, the anatase-rutile stability is especially sensitive when the mixture equivalence ratio (defined as the ratio of the actual fuel/oxygen ratio to the stoichiometric fuel/oxygen ratio) is near 1, i.e. a stochiometric mixture [21, 27, 28, 30, 32]. While the link between the oxygen environment and anatase-rutile relative stability is well established, the physical mechanisms behind it are not yet fully understood. The oxygen environment inevitably affects other synthesis conditions such as temperature and particle residence time. In addition, the formation of other metastable phases, such as TiO_2-B [40] and TiO_2-II [30], suggests that the current understanding of TiO_2 phase stability is incomplete.

Liu et al. [27] attempted to explain the effect of an oxidising environment by modifying the surface energy term in the thermodynamic model of Zhang and Banfield [53] to take into account the oxygen surface desorption. The underlying assumption is that the bulk structure of the particles remains unchanged, i.e. crystalline TiO_2. However, formation of stoichiometric incipient particles is unlikely. For example, Shmakov et al. [42] show that less-oxidised species such as Ti, TiO, Ti_2O_3 are formed initially in a TTIP-doped H_2/O_2/Ar flame. This is supported by a more recent experimental measurement that demonstrates that Ti and TiO are the main decomposition products of TTIP [13]. Buerger et al. [8] demonstrate that species such as TiH, $Ti(OH)_3$ are thermodynamically stable at flame temperature. These species are likely to constitute the incipient particles or clusters. For example, Fang et al. [14] detected $Ti_nO_xC_yN_z$ clusters with varying oxidation states of Ti which are thought to be the main building blocks of incipient particles in a TTIP-doped $CH_4/O_2/N_2$ flame. Lastly, the synthesised particles have been shown to contain oxygen defects in some cases, which likely originate from both surface and bulk [30, 44].

The formation of sub-oxide intermediates may play a key role in the anatase-rutile stability. Ishizuka et al. [19] performs an FT-IR study of TiO_2 nucleation from supersaturated vapours and observes oxygen-deficient oxides during the nucleation process. The degree of oxygen deficiency is expected to affect the anatase-rutile stability. In particular, rutile is known to better accommodate a high concentration of oxygen defects compared to anatase [6, 12]. For example, rutile can be easily reduced to form TiO_{2-x} crystals through formation of defect structures such as double charged oxygen vacancies, Ti interstitial, or planar defects [12, 23, 34]. The planar defect structure in the main rutile structure, a so-called crystallographic shear structure, is responsible for the formation of a homologous series of Magnéli phase which can be expressed as Ti_nO_{2n-1} with $n = 3,4,5,...$ [2, 35]. In rutile reduction experiments, a weight loss of more than 2% is shown to result in formation of lower oxides, Ti_3O_5 or Ti_2O_3 depending on the temperature [16].

The recent progress in modelling particle formation in laboratory-scale burners opens the possibility to use computational modelling to study processes that are challenging to observe experimentally. For example, Lindberg et al. [26] developed a detailed particle model in which the detailed morphologies of aggregates are tracked. This allows better understanding of the nano-structure of the particles formed in experiments [24, 25, 31]. In the current paper, the detailed of description of nanoparticles is further extended to include crystal phase information in order to better understand the phase formation mechanism.

The aim of this paper is to investigate the origin of the sensitivity of anatase-rutile stability in stoichiometric flames when the flame dilution is varied. This is done by comparing the model prediction to the experimental data. Surface energy and composition phase stability hypotheses are considered. A composition-dependent crossover size model is proposed in this work to explain the experimental observations. **This paper is structured as follows**. First, the relevant experimental methods and computational details are described briefly in Sections 2 and 3. The experimental data for phase composition and particle size are presented in Sections 4.1 and 4.2, respectively. Next, the origin of the anatase-rutile stability is discussed in Section 4.4 where surface energy-dependent stability (Section 4.4.1) and composition-dependent stability (Section 4.4.2) hypotheses are considered. Lastly, the conclusions are given in Section 5.

2 Experimental methods

The setup used to prepare the TiO_2 nanoparticles in this study has been described in our previous work [30]. This is similar to the setup used in other studies [32, 45, 46]. Briefly, a stoichiometric mixture of ethylene, oxygen, and argon as summarised in **Table 1**, was issued from a central aerodynamic nozzle with a total volumetric flow rate of 28 slpm. The nozzle had an exit diameter of 1.4 cm, resulting in an exit velocity of 436 cm/s at 150°C. The nozzle shape induced a flat plug flow of premixed gas that impinged on a stagnation surface. Titanium tetraisopropoxide (TTIP, $\geq 97\%$, Sigma-Aldrich) was injected into the unburned gas mixture with a syringe pump at 8 ml/h, corresponding to 365 ppm mole fraction. The gas line, precursor line, and burner surface were heated to 150°C to prevent TTIP condensation. During the experiment, the undoped flame was first stabilised for 15 minutes before TTIP was injected for 4 minutes. A shroud flow of 20 slpm N_2 gas was

used to stabilise and shield the jet flow from the ambient air.

Table 1: *The mixture fractions and equivalence ratio (ϕ) for all flames used in this study. T_{ad} and $X_{O_2,ad}$ are the adiabatic flame temperature and the equilibrium mole fraction of O_2 from the adiabatic simulations.*

Case	C_2H_4 (%)	O_2 (%)	Ar (%)	ϕ	T_{ad} (K)	$X_{O_2,\,ad}$
Flame 1	4.5	13.5	82.0	1.0	2419	0.91×10^{-2}
Flame 2	4.7	14.1	81.2	1.0	2453	1.04×10^{-2}
Flame 3	4.7	14.2	81.1	1.0	2457	1.05×10^{-2}
Flame 4	4.8	14.3	80.9	1.0	2466	1.09×10^{-2}
Flame 5	5.0	15.0	80.0	1.0	2500	1.24×10^{-2}
Flame 6	5.8	17.4	76.8	1.0	2603	1.78×10^{-2}

The stagnation surface was located 1 cm under the nozzle to stabilise the flame by flow stretch. Two configurations of stagnation surfaces were used. The first one was a rotating (300 rpm), circular stainless steel plate with its rotational axis located 10 cm from the burner centerline. Slots in the stagnation surface enabled the positioning of glass substrates while the plate rotation convectively cooled the substrate and the deposited particles. The deposition time for sample collection was 4 minutes. In the second configuration, a water-cooled non-rotating plate was used as the stagnation surface with a pinhole orifice for size measurements with a DMS500 fast particulate analyser. The details of the mobility size measurements and the dilution tests have been given elsewhere [31]. In both cases, a flat flame was stabilised at 3–4 mm above the stagnation plate depending on the flame mixture.

Powder X-ray diffraction (XRD) patterns of the collected samples were recorded with a D8 Advance diffractometer (Bruker) with Cu K_α radiation (40 kV, 30 mA). The 2θ scan range was 20–90° with a step size of 0.02° and 3 s per step. Zero-background silicon sample holders were used with powder samples pressed to create a dense and smooth film. The Rietveld refinement was performed with BRASS [5] using a simple size-strain broadening model, a spline-interpolated background, and experimental instrumental broadening parameters. Instrumental broadening parameters were obtained experimentally with standard reference material 640e from NIST. The structural parameters from the inorganic crystal structure database (ICSD) were used for anatase (no. 92363), rutile (no. 16636), TiO_2-B (no. 41056), and TiO_2-II (no. 158778).

3 Computational details

The adiabatic flame temperature is obtained from equilibrium simulations with constant pressure and enthalpy performed with the *k*inetics® software package [10]. The initial conditions are taken as the conditions of the premixed gas mixtures without TTIP in Table 1.

The particle formation in the flame was simulated using a two-step methodology [24].

In the first step, the flame structure, e.g., temperature profile and species composition, is modelled using a one-dimensional stagnation flow approximation, coupled to detailed gas-phase chemistry and a simple population balance model solved using method of moments with interpolative closure (MoMIC) as described by Manuputty et al. [29]. This is solved as a boundary-value problem using *k*inetics® [10]. The boundary conditions are specified according to the experimental conditions with an appropriate axial velocity gradient chosen to reproduce the experimental flame standing distance as discussed in [25].

In the second step, the resulting gas-phase profile is post-processed with the detailed particle model [26] to resolve the aggregate morphology and phase composition. The gas-phase profile, supplied as input to the population balance simulation, is expressed in terms of the residence time of a Lagrangian particle travelling from the burner to the stagnation plate using the combined convective and thermophoretic velocities. To account for the effect of thermophoretic transport near the stagnation surface, a thermophoretic correction is introduced to the post-process through a modified simulation sample volume scaling term. The post-processing methodology is described in detail in [24].

A stochastic numerical method is used to solve the population balance equations [26, 41]. The method employs a direct simulation algorithm with a majorant kernel and fictitious jumps [15, 37] to improve the computational speed of calculating the coagulation rate, and a linear process deferment algorithm [38] to provide an efficient treatment of sintering and surface growth. Simulation results are averaged over 4 runs, each with 8192 stochastic particles.

3.1 Gas-phase chemistry

The chemical reaction model consists of a TTIP decomposition mechanism combined with hydrocarbon combustion chemistry described by the USC-Mech II model [49]. The TTIP mechanism contains 25 Ti species and 61 reactions, and describes the decomposition of TTIP to titanium (IV) hydroxide ($Ti(OH)_4$) through the C_3H_6 and CH_3 abstraction pathways calculated by Buerger et al. [9] as well as dissociation reactions of $Ti(OH)_4$ to form small TiO_xH_y identified by Shmakov et al. [42] which are assumed to be barrierless due to the lack of available kinetics data. The mechanism has been published in the previous work [25]. These are summarised below.

$$\begin{aligned} \mathrm{TTIP} \longleftrightarrow \ldots \longleftrightarrow \mathrm{Ti(OH)_4} \\ \mathrm{Ti(OH)_4} \longleftrightarrow \mathrm{TiO_xH_y} \end{aligned}$$

3.2 Particle type space

Two particle models are used in this work: a univariate (simple) model used in the first simulation step and a multivariate (detailed) model used in the second step, i.e. post-processing. The simple particle model describes a particle by the number of constituent TiO_2 monomers [29] and ignores the effect of precursor species on the particle composition. The detailed particle model is described in detail in [26], so only a brief description

is given here.

An aggregate particle P_q containing $n_\mathrm{p}(P_q)$ primary particles is represented as

$$P_q = P_q\left(p_1, ..., p_{n_\mathrm{p}(P_q)}, \mathbf{C}\right), \tag{1}$$

where a primary particle p_i, with $i \in \{1, ..., n_\mathrm{p}(P_q)\}$, is represented by its internal coordinates

$$p_i = p_i\left(\eta, r, \mathbf{x}\right), \tag{2}$$

and the matrix $\mathbf{C}$ represents the primary particle connectivity. r is the radius of the primary, $\mathbf{x}$ is the position of the primary centre relative to the centre of mass of the aggregate and η is the primary composition. In the previous model [26], η describes the number of TiO_2 monomer. In this work, η describes the number of Ti and O atoms in each tracked phase. Three phases are considered here: anatase (An), rutile (Ru), and non-crystalline (NC), which encompasses melt or amorphous phase:

$$\eta = (\eta_{\mathrm{Ti,NC}}, \eta_{\mathrm{O,NC}}, \eta_{\mathrm{Ti,An}}, \eta_{\mathrm{O,An}}, \eta_{\mathrm{Ti,Ru}}, \eta_{\mathrm{O,Ru}}). \tag{3}$$

The oxygen to titanium ratio, $\sigma_{\mathrm{O},i}$, and the rutile fraction, $\mathrm{f}_{\mathrm{R},i}$, of particle i are calculated as follows,

$$\sigma_{\mathrm{O},i} = \frac{(\eta_\mathrm{O})_i}{(\eta_\mathrm{Ti})_i} = \frac{(\eta_{\mathrm{O,NC}})_i + (\eta_{\mathrm{O,An}})_i + (\eta_{\mathrm{O,Ru}})_i}{(\eta_{\mathrm{Ti,NC}})_i + (\eta_{\mathrm{Ti,An}})_i + (\eta_{\mathrm{Ti,Ru}})_i} \tag{4}$$

$$\mathrm{f}_{\mathrm{R},i} = \frac{(\eta_{\mathrm{Ti,Ru}})_i}{(\eta_\mathrm{Ti})_i} = \frac{(\eta_{\mathrm{Ti,Ru}})_i}{(\eta_{\mathrm{Ti,NC}})_i + (\eta_{\mathrm{Ti,An}})_i + (\eta_{\mathrm{Ti,Ru}})_i}. \tag{5}$$

3.3 Particle processes

The particle population evolves under the inception, surface growth, coagulation, sintering and coalescence processes described in [26]. Inception and surface growth are assumed to be collision limited. The rates of inception and surface growth are given by the free-molecular kernel with collision efficiencies γ_{IN} and γ_{SG} respectively. More detail on the treatment of the primary composition η during inception and surface growth with the collision species $Ti(OH)_3$ and $Ti(OH)_4$ is provided in Appendix A.

In this work the collision species and the growth rate parameters γ_{IN} and γ_{SG} are varied to investigate their influence on the predicted phase composition. These growth parameter sets are referred to in the rest of this work as $z^{(m)}$ with $m = 1, 2, 3$. These parameters are summarised in Table 2. The first set ($m = 1$) represents the parameters originally recommended in the previous work [25] using $Ti(OH)_4$ as the particle precursor. This model has been shown to compare reasonably well against the experimentally measured particle morphology (aggregate and primary particle sizes) for varying TTIP loadings and flame equivalence ratios. In the second set ($m = 2$), the same set of parameters were applied except both $Ti(OH)_4$ and $Ti(OH)_3$ species are used as precursor species. Lastly, to investigate the effect of the gas-phase chemistry on the phase formation, slower inception and surface growth are used in the third set ($m = 3$).

Table 2: *The growth parameters varied in this work ($z^{(m)}$, $m = 1,2,3$). Particle precursor is the species involved in inception and surface growth, γ_{IN} and γ_{SG} are the collision efficiencies for inception and surface growth processes.*

m	Particle precursor	γ_{IN}	γ_{SG}
1	$Ti(OH)_4$	1.0	1.0
2	$Ti(OH)_4$ and $Ti(OH)_3$	1.0	1.0
3	$Ti(OH)_4$ and $Ti(OH)_3$	1×10^{-3}	0.2

The rest of the particle model parameters used in this work are given in the appendix (Table 3). The rate of coagulation is given by the transition kernel [37] and the orientation and point of contact between the colliding particles is determined by ballistic cluster-cluster aggregation [20]. A molecular enhancement factor ε is applied to the free-molecular kernel for all collision processes. Sintering is described by a grain boundary diffusion model with parameters taken from [25]. In addition to the aforementioned particle processes, primary particles can also undergo a phase transformation, which is outlined below.

3.3.1 Phase transformation

A primary particle is able to undergo a temperature and size dependent phase transformation. This is treated as a discrete event that transforms the entire primary composition from one phase to another. The transformation event is independent from the processes described in Section 3.3, e.g., surface growth, sintering, coalescence, and therefore does not affect the particle morphology such as primary and aggregate sizes. The transformation event for primary particle i is controlled by two parameters: $T_{\mathrm{trans},i}$ and $d_{\mathrm{cross},i}$.

The transformation temperature $T_{\mathrm{trans},i}$ is the temperature at which a transformation occurs between the non-crystalline and crystalline phases. Meanwhile, a crossover diameter $d_{\mathrm{cross},i}$ determines which crystal phase is formed (anatase or rutile). The dependencies of parameters $T_{\mathrm{trans},i}$ and $d_{\mathrm{cross},i}$ vary depending on the submodel assumptions discussed in Sections 4.4.1 and 4.4.2.

Figure 1 shows the schematic for the phase transformation algorithm. Above the transformation temperature $T \geq T_{\mathrm{trans},i}$, the primary, containing η_{Ti} titanium and η_{O} oxygen atoms, is in a non-crystalline state. The composition vector of particle i is written as

$$\begin{aligned} \eta_i = (\eta_{\mathrm{Ti,NC}} = \eta_{\mathrm{Ti}}, \quad & \eta_{\mathrm{O,NC}} = \eta_{\mathrm{O}}, \\ \eta_{\mathrm{Ti,An}} = 0, \quad & \eta_{\mathrm{O,An}} =, \\ \eta_{\mathrm{Ti,Ru}} = 0, \quad & \eta_{\mathrm{O,Ru}} = 0). \end{aligned}$$

Below the transformation temperature $T < T_{\mathrm{trans},i}$ the non-crystalline primary transforms into a crystal phase (anatase or rutile) determined by the primary size $d_{\mathrm{p},i}$. The primary size $d_{\mathrm{p},i}$ is assumed to be the spherical equivalent diameter. Below the crossover diameter $d_{\mathrm{p},i} < d_{\mathrm{cross},i}$, the primary is assumed to transform into anatase, so that the primary

composition is now

$$\begin{aligned}\eta_i = (\eta_{\mathrm{Ti,NC}} = 0, \quad & \eta_{\mathrm{O,NC}} = 0,\\ \eta_{\mathrm{Ti,An}} = \eta_{\mathrm{Ti}}, \quad & \eta_{\mathrm{O,An}} = \eta_{\mathrm{O}},\\ \eta_{\mathrm{Ti,Ru}} = 0, \quad & \eta_{\mathrm{O,Ru}} = 0),\end{aligned}$$

while above the crossover diameter $d_{\mathrm{p},i} \geq d_{\mathrm{cross},i}$, the primary transforms into rutile:

$$\begin{aligned}\eta_i = (\eta_{\mathrm{Ti,NC}} = 0, \quad & \eta_{\mathrm{O,NC}} = 0,\\ \eta_{\mathrm{Ti,An}} = 0, \quad & \eta_{\mathrm{O,An}} = 0,\\ \eta_{\mathrm{Ti,Ru}} = \eta_{\mathrm{Ti}}, \quad & \eta_{\mathrm{O,Ru}} = \eta_{\mathrm{O}}).\end{aligned}$$

Further, a simplifying assumption is made here that the phase transformation between anatase and rutile is negligible due to the fast cooling rate of the particles near the stagnation plate. Thus, the crystallite growth after solidification is only determined by surface growth.

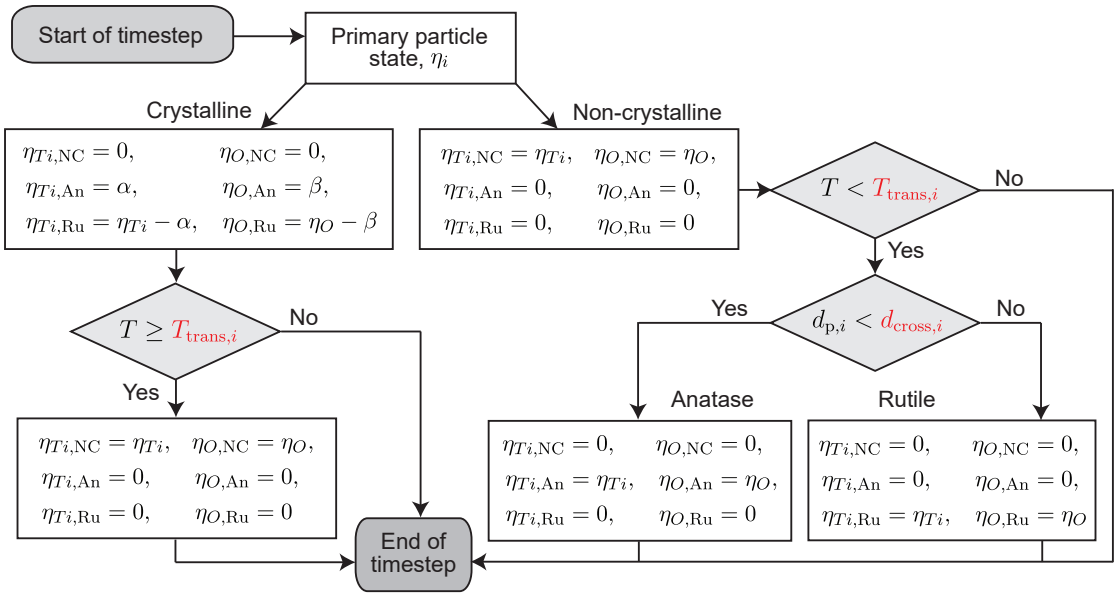

Figure 1: *Phase transformation algorithm. $T_{\mathrm{trans},i}$ and $d_{\mathrm{cross},i}$ (shown in red) are a function of the model parameter vector θ which is defined in the submodel description.*

3.4 Parameter estimation

The amount of each phase in primary particle i is determined by y (a vector of flame conditions), z (a vector of growth parameters in Table 2, not optimised in this study), $d_{\mathrm{cross},i}$, and $T_{\mathrm{trans},i}$. The total amount of each phase at the end of the simulations, n_{NC}, n_{A},

n_{R} can be represented by functions g_{NC}, g_{A}, and g_{R} as follows,

$$n_{\mathrm{NC}} = \sum_{i=i}^{N} (\eta_{\mathrm{Ti,NC}})_i = \sum_{i=i}^{N} g_{\mathrm{NC}}(y; z, d_{\mathrm{cross},i}, T_{\mathrm{trans},i}) \tag{6}$$

$$n_{\mathrm{A}} = \sum_{i=i}^{N} (\eta_{\mathrm{Ti,An}})_i = \sum_{i=i}^{N} g_{\mathrm{A}}(y; z, d_{\mathrm{cross},i}, T_{\mathrm{trans},i}) \tag{7}$$

$$n_{\mathrm{R}} = \sum_{i=i}^{N} (\eta_{\mathrm{Ti,Ru}})_i = \sum_{i=i}^{N} g_{\mathrm{R}}(y; z, d_{\mathrm{cross},i}, T_{\mathrm{trans},i}), \tag{8}$$

where N is the total number of primary particles in the simulation. The rutile fraction, $\mathrm{f_R}$, is given by a function f,

$$\mathrm{f_R} = \frac{n_{\mathrm{R}}}{n_{\mathrm{NC}} + n_{\mathrm{A}} + n_{\mathrm{R}}} = f(y; z, \theta). \tag{9}$$

where θ is a vector containing the dependencies of $d_{\mathrm{cross},i}$, and $T_{\mathrm{trans},i}$ which is optimised in this study.

The best parameter set $\hat{\theta}_m$ for the growth parameter set m (see Table 2) is evaluated as follows

$$\hat{\theta}_m = \arg\min_{\theta} \sum_{j=1}^{N_{\mathrm{exp}}} (f(y^{(j)}; z^{(m)}, \theta) - \mathrm{f_R^{exp,(j)}})^2, \tag{10}$$

where the $y^{(i)}$ is a vector of process conditions for flame i, $z^{(m)}$ is a vector of growth parameters in case m (see Table 2), $\mathrm{f_R^{exp}}$ is the experimentally measured rutile fraction from flame i, and N_{exp} is the number of flame conditions tested which is 6 in this study.

4 Results and discussion

4.1 Phase composition

Figure 2 summarises the results of the experimental phase quantification. The XRD patterns for samples prepared in flames 1–6 are shown in **Fig. 2(a)**. The patterns are deconvoluted with the Rietveld refinement (full profile fitting) using four TiO_2 phases: Rutile (R), anatase (A), bronze (B) and TiO_2-II (II). These four phases have previously been identified in similar flames through XRD pattern analysis as well as high-resolution TEM images and electron diffraction patterns [30]. The broad peaks of all four phases suggest that the crystallites are nano-sized with possible microstrain present although no size/strain analysis is attempted here due to the high degree of peak overlap and the resulting uncertainty in the fitting.

Figure 2(b) shows the phase composition of all samples obtained from the refinement. While the content of metastable TiO_2-B and TiO_2-II phases are nearly constant, the anatase content gradually decreases while rutile increases from flames 1 to 6, i.e. decreasing flame

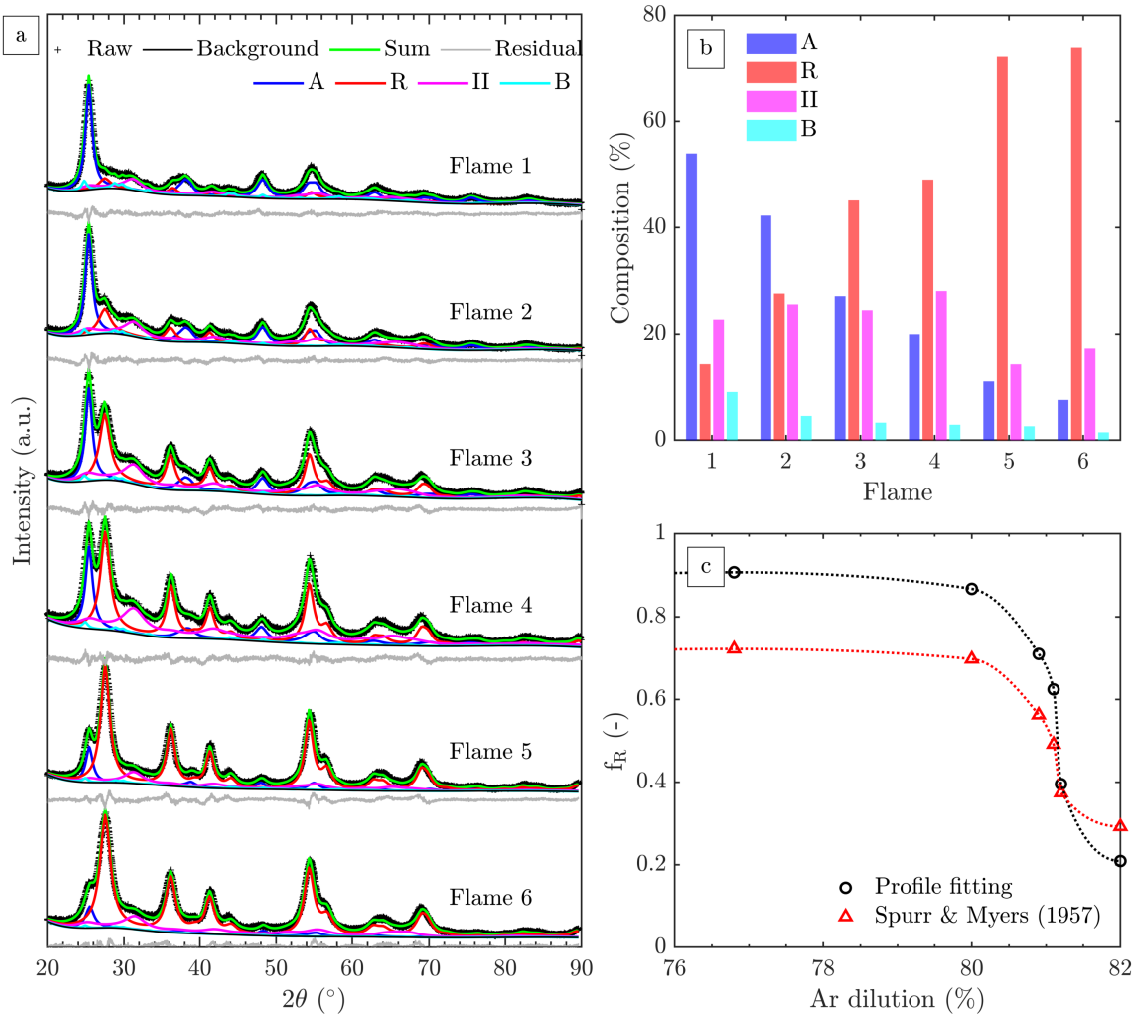

Figure 2: *(a) Powder XRD patterns of samples prepared in flames 1–6 and the individual phase profiles obtained from the Rietveld refinement, (b) Phase composition of samples prepared in flames 1–6, (c) Rietveld-determined rutile fraction (relative to anatase and rutile total),* f_R*, compared to the empirical relationship of Spurr and Myers [43] as a function of Ar dilution. The lines are added as a visual aid.*

dilution. This trend demonstrates a strong sensitivity of anatase-rutile stability as a function of mixture dilution. This agrees well with previous experimental observations where anatase-rutile stability was observed to change dramatically near the stoichiometric point [21, 28, 30].

As the aim of this work is to investigate the origin of anatase-rutile stability, the metastable phases TiO_2-B and TiO_2-II are excluded from the rutile fraction calculation. Nevertheless, the fractions of these phases are not negligible (up to 30% in total) – the consequence of this is discussed further in Section 4.4.2. **Figure 2(c)** shows the relative rutile content, f_R = R/(A+R), where R and A denote the rutile and anatase fractions from the refinement as a function of the Ar dilution. The result shows a high sensitivity of anatase-rutile

stability at Ar dilution of $\approx 81\%$. In addition, an estimation of f_R using the empirical relationship given by Spurr and Myers [43] is shown. The comparison shows a difference of up to 20% between the two methods. This is not surprising as the formula proposed by Spurr and Myers [43] was determined using XRD patterns for powder samples with crystallite size of approximately 50-500 nm with much less broadening compared to the present results. Further, only anatase and rutile were present in their powder sample compared to the four phases in the this work.

The presence of the metastable polymorphs indicates a limited phase transformation of the deposited particles on the rotating surface. This is due to the rapid quenching of the formed particles near the stagnation plate. For example, we showed previously that the TiO_2-II phase eventually transforms to rutile upon prolonged exposure to the flame (when a non-rotating stagnation plate was used) [30].

Ma and Yang [28] previously demonstrated the effect of the premixed gas dilution (with N_2) on the anatase-rutile stability of TiO_2 prepared in a bunsen burner and showed a trend that is the opposite of the data in Fig. 2(c). In their study, increasing Ar dilution results in a higher rutile fraction. They suggest that this trend is due to a faster anatase-rutile transformation in oxygen lean environments as the initial oxygen content is lower in more diluted flames. It should be noted that the samples in their study were collected from 3 cm and 5 cm above the burner (Figs. 6 and 7 in [28]), corresponding to an estimated residence time of 25–60 ms (estimated based on the process conditions reported as no residence time calculation was given). This is in contrast with the residence time of 3–5 ms estimated for the flames used in this study [30]. The longer residence time in Ref. [28] compared to this study is consistent with the particle size (20-500 nm) that is much larger than reported here (7–8 nm, discussed in the next section). Thus, it is suggested that the sensitivity shown in Fig. 2(c) is pertinent to the very early stages of particle formation and does not necessarily contradict the results reported by Ma and Yang [28].

4.2 Particle size distributions

Figure 3(a) shows the measured aggregate mobility sizes for all flames. The aggregate sizes are similar for the different flame conditions (flames 1–6). This is consistent with our previous work where we demonstrated that the particle sizes are not sensitive to the flame distance/equivalence ratio due to the compensating effect between temperature and particle residence time [25, 31].

The simulated aggregate size (spherical equivalent size from projected area analysis) for three cases considered in this work (see Table 2) are also presented in shown Fig. 3(a). The validity of comparing the experimentally measured mobility aggregate size with the simulated spherical equivalent size has been discussed elsewhere [31]. The predicted aggregate sizes compare well with the measured aggregate size. In addition, the results for the three different growth parameter sets considered (Table 2) are very similar, suggesting that the particle morphology is insensitive to the choice of precursor species and the gas-phase chemistry. This is consistent with the numerical sensitivity tests performed by Lindberg et al. [25].

The predicted mean primary particle size is shown in **Fig. 3(b)**. The primary particle size

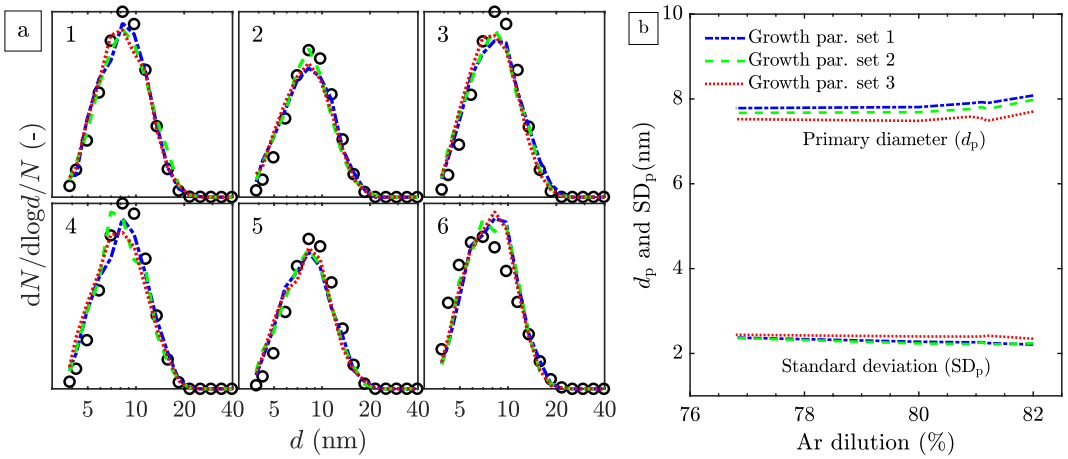

Figure 3: *Particle sizes at the stagnation point: (a) Measured and simulated aggregate size distributions, (b) simulated mean primary particle size, d_p, and the standard deviations, SD_p, as a function of Ar dilution. The measured data is shown in symbols, simulated data is shown with lines. For description of growth parameter sets 1–3, see Table 2.*

increases slightly with increasing Ar dilution, at around ~ 8 nm, which is in a good agreement with previous primary particle size measurements with TEM [30, 31] (the primary particle sizes for 4 and 12 ml/h TTIP loading were 6 and 9 nm, respectively).

4.3 Flame structure

The one-dimensional stagnation flow approximation was used to estimate the temperature and other flame structure information. **Figures 4(a) and 4(b)** show the simulated temperature and oxygen mole fraction profiles for flames 1–6. It shows that flames 1–6 differ mainly in the location of their flame front, which is consistent with the experimentally observed luminous flame location. In addition, the flames differ in their maximum temperature (and consequently particle time-temperature history).

The maximum flame temperature varies by approximately 300°C between flames 1 and 6, similar to the difference of the calculated adiabatic flame temperature as summarised in Table 1. The oxygen mole fraction initially varies between flames 1–6 as a consequence of the difference in the diluent gas (Ar) fraction. In the post-flame region, however, the O_2 mole fractions show little variation across the flames at approximately 1×10^{-2}. This value is comparable to the adiabatic O_2 mole fraction obtained from the equilibrium simulation (Table 1).

4.4 Origin of anatase-rutile stability

The origin of the dramatic shift in the anatase-rutile composition as a function of flame dilution (Fig. 2(c)) is examined by considering two main formation pathways as illustrated in a simplified phase diagram in **Fig. 5**. The **first pathway** assumes a stoichiometric

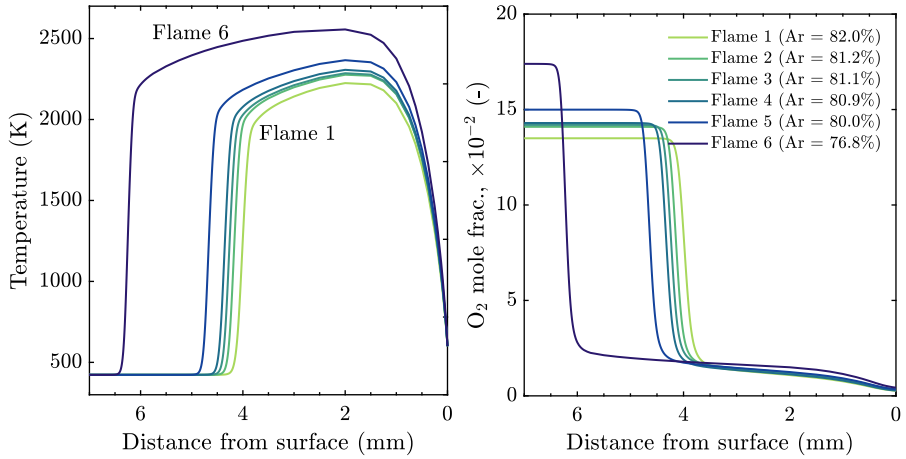

Figure 4: *The simulated flame structure for flames 1–6: (a) temperature and (b) O_2 mole fraction profiles.*

composition at the point of crystallisation. In this case, a thermodynamic analysis similar to the approach by Zhang and Banfield [53, 54] can be applied resulting in a crossover size at which anatase and rutile are switched. This crossover size is a function of the surface energy. Thus, pathway 1 is referred to as the surface energy-dependent hypothesis. In the **second pathway**, rapid clustering and cooling result in a non-stoichiometric melt which solidifies to form sub-oxides. The sub-oxides are hypothesised to preferentially transform to rutile due to the similarity in their structures. Thus, in this pathway the anatase-rutile crossover size is determined by the composition of the intermediates, i.e. composition-dependent hypothesis. It is important to note that the analysis given here only takes into account anatase and rutile while ignoring the other metastable phases and is therefore only qualitative in nature. More importantly, the question this analysis seeks to answer is: *given the variation in the flame conditions (dilution with Ar), can the trend of anatase-to-rutile ratio be explained by a size-dependent model which is driven by surface energy (pathway 1) and/or particle composition (pathway 2)*?

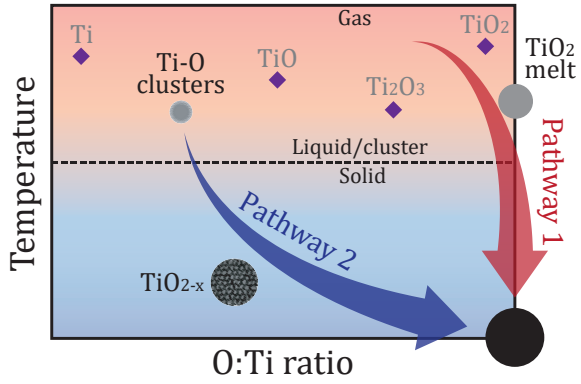

Figure 5: *A schematic illustrating two TiO_2 formation pathways.*

4.4.1 Pathway 1: Surface energy-dependent crossover size

The surface energy-dependency of the anatase-rutile crossover size can be explained in two ways or models. The first model is motivated by the thermodynamic analysis of Zhang and Banfield [53, 54]. This approach is termed the **Gibbs energy model** as the crossover size arises from the formulation of anatase-rutile transformation Gibbs energy by taking into account contributions from the surface free energy and surface stress of crystalline nanoparticles. In the second model, the crossover size arises when cooling of melt is considered following the approach of Guisbiers et al. [18]. In this case, the phase with the higher melting point, which is a function of particle size, solidifies first and is stabilised. This is subsequently termed the **melting model**.

Gibbs energy model

Following the thermodynamic analysis of Zhang and Banfield [53, 54], the anatase-rutile transformation Gibbs free energy, $\Delta G^{\circ}_{\mathrm{A}\to\mathrm{R}}$, is determined by a few thermodynamic quantities including the bulk Gibbs energies and surface free energy,

$$\Delta G^{\circ}_{\mathrm{A}\to\mathrm{R}} = \Delta G^{\circ}_{f,\mathrm{R}} - \Delta G^{\circ}_{f,\mathrm{A}} + 2(2t+3)\frac{M}{d}\left(\frac{\gamma_{\mathrm{R}}}{\rho_{\mathrm{R}}} - \frac{\gamma_{\mathrm{A}}}{\rho_{\mathrm{A}}}\right), \tag{11}$$

where $\Delta G^{\circ}_{f,\mathrm{R}}$ and $\Delta G^{\circ}_{f,\mathrm{A}}$ are the Gibbs free energies of formation of rutile and anatase, t is the ratio of surface stress to surface free energy, M is the molar mass of TiO_2, $d = 2r$ is the crystalite size, ρ_{R} and ρ_{A} are the mass densities of rutile and anatase, γ_{R} and γ_{A} are the surface free energies of rutile and anatase. In general, the term $\Delta G^{\circ}_{f,\mathrm{R}} - \Delta G^{\circ}_{f,\mathrm{A}}$ is negative (rutile is thermodynamically more stable for bulk) while the second term $\gamma_{\mathrm{R}}/\rho_{\mathrm{R}} - \gamma_{\mathrm{A}}/\rho_{\mathrm{A}}$ is positive (anatase has lower surface energy). Thus,

$$\Delta G^{\circ}_{\mathrm{A}\to\mathrm{R}} \begin{cases} > 0 \text{ (anatase is more stable)}, & \text{for } d < d_0 \\ = 0 \text{ (equilibrium)}, & \text{for } d = d_0 \\ < 0 \text{ (rutile is more stable)}, & \text{for } d > d_0 \end{cases}, \tag{12}$$

where d_0 is the size at which anatase and rutile are thermodynamically in equilibrium. d_0 is thus determined by the thermodynamic quantities in Eq. 11, i.e.

$$d_0 = d_0(\Delta G^{\circ}_{f,\mathrm{A}}, \Delta G^{\circ}_{f,\mathrm{A}}, t, M, \gamma_{\mathrm{A}}, \gamma_{\mathrm{R}}, \rho_{\mathrm{A}}, \rho_{\mathrm{R}}). \tag{13}$$

Precise determination of the surface free energy is challenging for a few reasons. First, nanoparticles may undergo significant surface reconstructions resulting in a lower surface free energy compared to that of clean-cut surface. The surface reconstruction itself is expected to vary with particle size which results in size-dependent surface free energies [33]. Second, the surface energetics are heavily affected by the chemical environments, e.g., degree of hydrogenation and adsorbed species [3, 4]. The uncertainty of the surface energies leads to a massive uncertainty in calculation of d_0 as the nominal values of $\gamma_{\mathrm{R}}/\rho_{\mathrm{R}}$ and $\gamma_{\mathrm{A}}/\rho_{\mathrm{A}}$ are close (see the last term in Eq. 11). This explains the large uncertainty of surface energies found in the literature both calculated and experimentally measured [39].

For example, with the surface energies found in the literature, a critical size of anywhere between 2 to 50 nm can be justified using Eq. 11.

The uncertainties in the thermodynamic quantities motivate the choice of imposing d_0 directly as a free parameter in this model. It is also noted that the quantities in Eq. 11, e.g., $\Delta G^{\circ}_{f,\mathrm{A}}$, $\Delta G^{\circ}_{f,\mathrm{A}}$, t, γ_{A}, γ_{R}, ρ_{A}, ρ_{R} are temperature dependent but the overall temperature dependence of $\Delta G^{\circ}_{\mathrm{A}\to\mathrm{R}}$ is often assumed to be negligible due to the difference terms. Therefore, $d_{\mathrm{cross},i}$ can now be written as

$$d_{\mathrm{cross},i} = d_0 = \alpha_1, \tag{14}$$

where α_1 is a constant and a free model parameter.

The anatase-rutile stability given by $\Delta G^{\circ}_{\mathrm{A}\to\mathrm{R}}$ only considers the thermodynamic stability. In order to account for the kinetic effect, another model parameter α_2 is introduced such that the transformation as dictated by the thermodynamic stability only occurs (simultaneously) when $T \geq \alpha_2$ and completely arrested when $T < \alpha_2$. Therefore,

$$T_{\mathrm{trans},i} = \alpha_2. \tag{15}$$

The rutile fraction function in Eq. 9 is now written as

$$\mathrm{f_R} = f_{\mathrm{Gibbs}}(y; z, \theta) \quad \text{where } \theta = [\alpha_1, \alpha_2]. \tag{16}$$

Figure 6(a) shows the predicted rutile fraction as a function of the parameters α_1 and α_2 according to Eq. 16 for flame 1 and growth parameter set 1 (see Table 2). Qualitatively, the model responses are very similar for all flames and growth parameter sets tested. This is a consequence of the similarity in the simulated size-temperature trajectories of the particles. As the crossover size (α_1) increases the rutile fraction decreases as expected. The rutile fraction is less sensitive to the transformation temperature (α_2). This is due to the high cooling rates near the stagnation plate where the particle growth is limited.

The best fit parameters for the Gibbs energy model are calculated according to Eq. 10 for $\alpha_1 = [4\ \ 12]$ nm and $\alpha_1 = [1500\ \ 2000]$ K. An upperlimit of 2000 K for α_1 is used considering the melting point of bulk anatase is 2075 K. **Figure 6(b)** shows the measured and predicted rutile fractions with these fitted parameters for the three growth parameter sets in Table 2. The fitted parameters $\hat{\theta}_m$ are very similar for all growth parameters used ($m = 1, 2, 3$). This is not surprising as the particles sizes are insensitive to the growth parameters as shown in Fig. 3. The fitted crossover size is $\sim$7 nm which is smaller than the crossover size calculated by Zhang and Banfield [53] (14 nm). The Gibbs energy model correctly predicts a decreasing rutile fraction trend with increasing Ar dilution albeit with a much weaker sensitivity compared to the measurements.

Melting model

In the Gibbs model, the effect of particle polydispersity on the transformation temperature is neglected (Eq. 15). The particle polydispersity can be accounted for in the melting model by assuming that the transformation temperature is equal to the melting point.

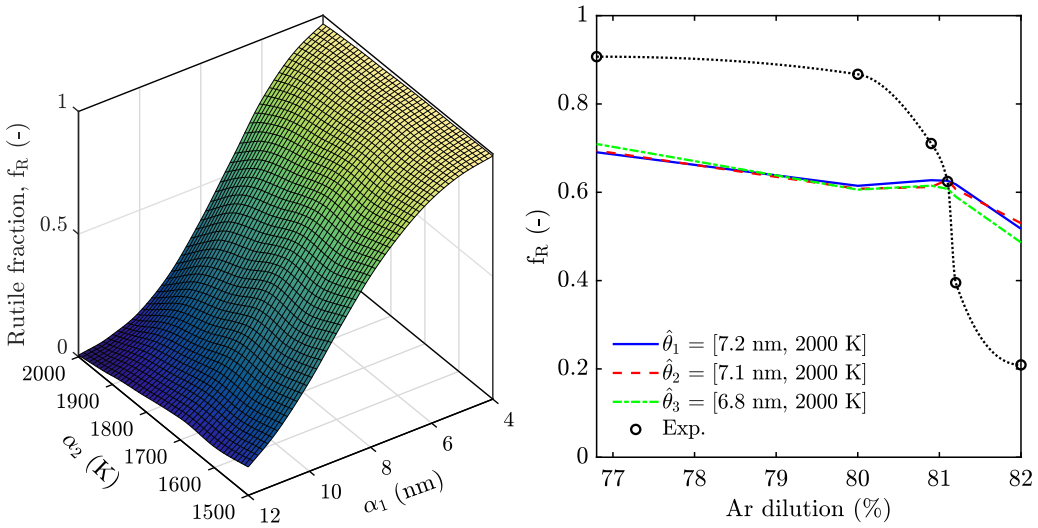

Figure 6: *(a) The predicted rutile fraction,* $f_R = f_{Gibbs}(y^{(1)}; z^{(1)}, \theta)$ *with* $\theta = [\alpha_1, \alpha_2]$*, for flame 1 (Ar = 82.0%) and growth parameter set 1 (see Table 2), according to the Gibbs energy model. (b) The measured and predicted rutile fractions as a function of Ar dilution with the best fit parameters* $\hat{\theta}_1$*,* $\hat{\theta}_2$*, and* $\hat{\theta}_3$ *according to Eq. 10. The line is added to the experimental data as a visual aid.*

Following the approach by Guisbiers et al. [18], the melting point of a particle with size d, T_d^m, can be expressed as

$$\frac{T_d^m}{T_\infty^m} = 1 - \frac{\gamma_s - \gamma_l}{\Delta H_{m,\infty}} \frac{A}{V} = 1 - \frac{\beta}{d}, \tag{17}$$

T_∞^{melt} is the bulk melting point, γ_s and γ_l are the solid and liquid surface energies, and $\Delta H_{m,\infty}$ is the bulk melting enthalpy. Similar to the Gibbs energy model, the thermodynamic quantities are subject to massive uncertainties and thus are treated as a model parameter β (β_1 for anatase and β_2 for rutile).

Rutile has a higher melting point than anatase ($T_{\infty,An}^m = 2075$ K for anatase, $T_{\infty,Ru}^m = 2143$ K for rutile [18]). Therefore, for $\beta_1 < \beta_2$ the melting points of anatase and rutile intersect at $T_{d,Ru}^m = T_{d,An}^m = T^*$ and $d = d^*$. For example, **Fig. 7** shows the melting points of anatase and rutile as a function of $1/d$ for $\beta_1 = 2.0$ nm and $\beta_2 = 2.5$ nm.

For a melt with size d, the solidification will occur at $T = T_d^m$ given by

$$T_d^m = \max\left(T_{d,An}^m, T_{d,Ru}^m\right). \tag{18}$$

Assuming phase transformation only occurs at the solidification point, the transformation temperature for particle i, $T_{trans,i}$, is equal to $T_{d_i}^m$ and is defined by a function h_1,

$$T_{trans,i} = T_{d_i}^m = h_1(\beta_1, \beta_2, d_i), \tag{19}$$

where

$$h_1(\beta_1, \beta_2, d_i) = \max\left(\left[T_{\infty,An}^m\left(1 - \frac{\beta_1}{d_i}\right)\right], \left[T_{\infty,Ru}^m\left(1 - \frac{\beta_2}{d_i}\right)\right]\right) \tag{20}$$

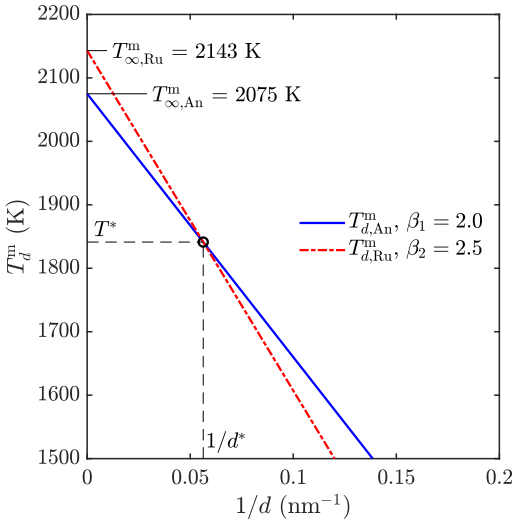

Figure 7: *The melting points of anatase and rutile as a function of reciprocal particle size. When $\beta_1 < \beta_2$, the two melting points intersect at $T^{\mathrm{m}}_{d,\mathrm{Ru}} = T^{\mathrm{m}}_{d,\mathrm{An}} = T^*$ and $d = d^*$.*

Meanwhile, the crossover size for particle i, $d_{\mathrm{cross},i}$, is equal to d^*,

$$d_{\mathrm{cross},i} = d^* = h_2(\beta_1, \beta_2), \tag{21}$$

where

$$h_2(\beta_1, \beta_2) = \frac{T^{\mathrm{m}}_{\infty,\mathrm{Ru}}\beta_2 - T^{\mathrm{m}}_{\infty,\mathrm{An}}\beta_1}{T^{\mathrm{m}}_{\infty,\mathrm{Ru}} - T^{\mathrm{m}}_{\infty,\mathrm{An}}}. \tag{22}$$

Finally, the rutile fraction function in Eq. 9 is now written as

$$\mathrm{f_R} = f_{\mathrm{melt}}(y; z, \theta) \quad \text{where } \theta = [\beta_1, \beta_2], \tag{23}$$

where β_1 and β_2 are the free model parameters.

For easier comparison to the Gibbs energy model, the function $f_{\mathrm{melt}}(x;\theta)$ can be transformed to $f^*_{\mathrm{melt}}(x;\theta^*)$ as follows

$$f_{\mathrm{melt}}(y; z, \theta) = f^*_{\mathrm{melt}}(y; z, \theta^*) \quad \text{where } \theta^* = [d^*, T^*], \tag{24}$$

where d^* is the crossover diameter, given by $h_2(\beta_1, \beta_2)$ in Eq. 22, and T^* is the melting point of particle with size d^*, given by $h_3(\beta_1, \beta_2)$ below,

$$T^* = h_3(\beta_1, \beta_2) = \frac{\beta_2 - \beta_1}{\beta_2/T^{\mathrm{m}}_{\infty,\mathrm{An}} - \beta_1/T^{\mathrm{m}}_{\infty,\mathrm{Ru}}}, \tag{25}$$

Figure 8(a) shows the predicted rutile fraction as a function of the parameters d^* and T^* according to Eq. 24 for flame 1 and growth parameter set 1 (see Table 2). Interestingly the model response is very similar to the Gibbs energy model. This suggests that the effect

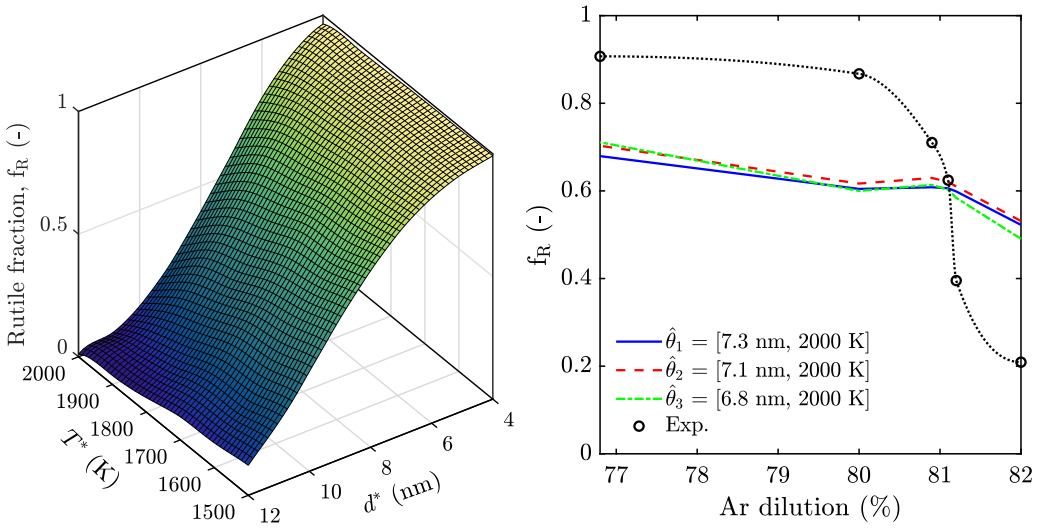

Figure 8: *(a) The predicted rutile fraction,* $f_R = f^*_{melt}(y^{(1)}; z^{(1)}, \theta^*)$ *with* $\theta^* = [d^*, T^*]$*, for flame 1 (Ar = 82.0%) and case 1 (see Table 2), according to the melting model. (b) The measured and predicted rutile fractions as a function of Ar dilution with the best fit parameters* $\hat{\theta}_1$*,* $\hat{\theta}_2$*, and* $\hat{\theta}_3$ *according to Eq. 10. The line is added to the experimental data as a visual aid.*

of particle polydispersity is not very important for the cases considered here. This is a result of the narrow particle size distribution as shown by the small standard deviations in Fig. 3(b).

The similarity between the melting and the Gibbs energy models are further shown by the predicted rutile fractions in **Fig. 8(b)** (compared to Fig. 6(b)). The best fit parameters for the melting model are calculated according to Eq. 10 for $d^* = [4\ \ 12]$ nm and $T^* = [1500\ \ 2000]$ K. The fitted parameters $d^* = 7$ nm and $T^* = 2000$ K are equivalent to $\beta_1 = 0.253$ nm and $\beta_2 = 0.467$ nm asccording to Eqs. 21, 22, and 25. These are much smaller than the values calculated by Guisbiers et al. [18] ($\beta_1 = 1.27$ nm and $\beta_2 = 2.58$ nm) using the surface energies obtained from using molecular dynamic simulations for anatase and rutile with clean cut surfaces [36]. Using their reported values for β_1 and β_2, the predicted crossover size is ~ 40 nm. This suggests that the surface energies of the particles formed in flames are much smaller than those calculated for the cut surfaces. Nevertheless, similar to the Gibbs energy model, the sensitivity of the rutile fraction as a function of Ar dilution predicted by the melting model is much weaker than the trend from the measurements.

4.4.2 Pathway 2: Composition-dependent crossover size

In the second pathway, the sensitivity of the anatase-rutile ratio as a function of the dilution ratio is explained by considering the effect of flame temperature (Fig. 4(a)) on the particle composition. The flame temperature affects the gas-phase chemistry of the particle precursor species and subsequently the particle composition.

The hypothesis is that the nascent particles are oxygen deficient, i.e. TiO_{2-x}, and the anatase or rutile formation is controlled by their oxygen content. This is motivated by the

experimental observations where rutile is formed in oxygen-lean and anatase in oxygen-rich environments [21, 27]. In a similar way, doping of trivalent ions such as Al, Cr, Fe that create oxygen defects have long been used to promote the formation of rutile over anatase in gas-phase synthesis [1, 48, 52].

The implied assumption is that particle solidification/crystal structure formation occurs at a faster rate than the oxidation of TiO_{2-x} clusters as shown in pathway 2 in Fig. 5. These nascent clusters are likely to be amorphous as demonstrated by molecular dynamic studies for TiO_2 particles smaller than 2 nm [54]. Formation of oxygen vacancies in amorphous TiO_2 is expected to be easier than in crystalline titania [11]. Teleki and Pratsinis [44] also show that highly oxygen deficient TiO_2 particles, possibly even suboxides, are formed in flame synthesis conditions. The oxygen vacancies explain the blue appearance of powders prepared in oxygen lean environments (which usually has high rutile content) [30].

In reality, the initial clusters are likely to be very complex and possibly contain unreacted hydrocarbon fragments (also nitrogen when present) such as those detected in time-of-flight mass spectrometer measurements [14, 50]. Here we only consider TiO_xH_y (1 Ti centre) species which are assumed to undergo a complete dehydration during inception and condensation reactions (Section 3.3). Thus, the oxygen content in the particle is solely controlled by the implied oxidation state of the gas-phase particle precursor.

Gas-phase precursors

Figure 9 shows the simulated mole fractions of TTIP and small Ti-containing species TiO_xH_y considered in the gas-phase mechanism used here for the growth parameter sets considered (Table 2). Among all species, only $Ti(OH)_4$ and $Ti(OH)_3$ are present in significant concentration. This is not surprising as $Ti(OH)_4$ is the final product of the TTIP decomposition mechanism and $Ti(OH)_3$ is formed from direct reactions of $Ti(OH)_4$. These two species have also been detected by Fang et al. [14] in TTIP-doped $CH_4/O_2/N_2$ flames. The importance of $Ti(OH)_4$ and $Ti(OH)_3$ motivates the choice of these species as the precursor species in the particle model (see Section 3.3).

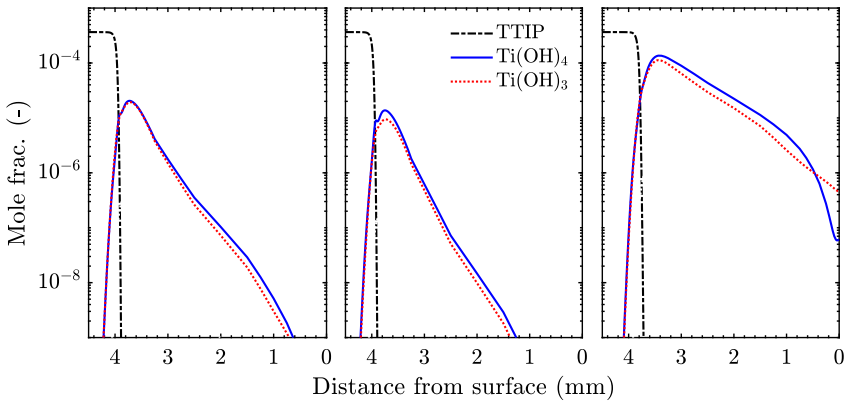

Figure 9: *The simulated mole fractions of TTIP and small Ti-containing species TiO_xH_y (post-$Ti(OH)_4$) for flame 1 using different growth parameter sets: set 1 (left), 2 (middle), 3 (right). For description of growth parameter sets 1–3, see Table 2.*

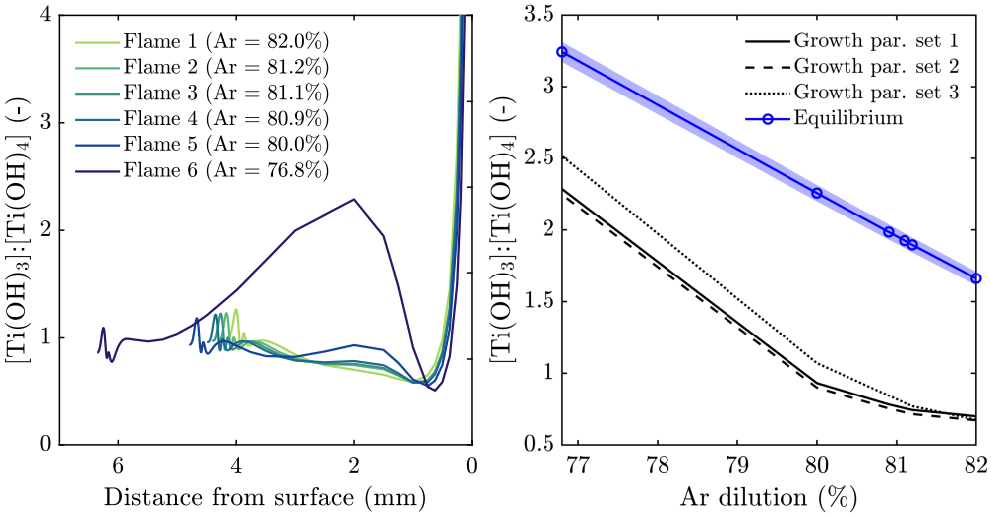

Figure 10: *(a) The ratio of $Ti(OH)_3$ to $Ti(OH)_4$ simulated mole fractions for flames 1–6 with growth parameter set 1. The start of the lines correspond to the flame fronts (defined as $T = 500$ K). The small oscillations near the flame front are caused by the particle inception. (b) The ratio of $Ti(OH)_3$ to $Ti(OH)_4$ mole fractions at the maximum flame temperature as a function of Ar dilution (lines) for the different growth parameter sets. The symbols are from the equilibrium simulations. The shaded area represents the equilibrium ratio for mixtures with equivalence ratio of* 1.00 ± 0.01. *For description of growth parameter sets 1–3, see Table 2.*

Figure 10(a) shows the difference in the ratio of $Ti(OH)_3$ to $Ti(OH)_4$ for flames 1–6. The variation in Fig. 10(a) is most pronounced in the post flame region around 2 mm from the stagnation plate. The difference in this maximum ratio represents an equilibrium shift in the gas phase due to the increasing maximum temperature from flames 1 to 6. This is demonstrated in **Fig. 10(b)** where the ratio of $Ti(OH)_3$ to $Ti(OH)_4$ at the maximum temperature for each flame (approximately 1.5–2 mm based on Fig. 4(a)) is plotted for the different growth parameter sets (Table 2). This shows that the trend of the relative ratio of $Ti(OH)_3$ to $Ti(OH)_4$ is insensitive to the growth parameters used and is consistent with the trend from the equilibrium simulations. A similar observation was reported by Buerger et al. [8] where increasing temperature shifts the equilibrium from $Ti(OH)_4$ to $Ti(OH)_3$. The difference between the flames and the equilibrium simulations is attributed to the difference between the maximum flame temperature (Fig. 4(a)) and the adiabatic flame temperature (Table 1). The sensitivity of the $Ti(OH)_3$ to $Ti(OH)_4$ equilibrium ratio to the mixture equivalence ratio is shown by the shaded region. The uncertainty of 1.00 ± 0.01 is expected due to the uncertainty in the experimental flowrates.

Particle composition

$Ti(OH)_4$ and $Ti(OH)_3$ have different implied oxidation states of Ti, i.e. +4 and +3 respectively. Assuming the inception and surface growth preserve the oxidation state of Ti of

the precursor by the release of water, the particle formation can be written as

$$\mathrm{Ti(OH)_{4(gas)} \longrightarrow TiO_{2(particle)} + 2\,H_2O_{(gas)}}$$
$$\mathrm{Ti(OH)_{3(gas)} \longrightarrow TiO_{1.5(particle)} + 1.5\,H_2O_{(gas)}}.$$

Therefore, the relative amount of $Ti(OH)_4$ and $Ti(OH)_3$ strongly affects the oxygen to titanium ratio in the particles, σ_O.

In the gas-phase mechanism used in this study, $Ti(OH)_4$ decomposes to form $Ti(OH)_3$ through a OH-abstraction. This reaction competes with the inception and surface growth processes. Therefore, the particle formation rate will also impact the particle composition (σ_O). The growth parameter set 3 (see Table 2) is included here to investigate this, i.e. set 3 assumes slower inception and surface growth compared to set 2.

The oxygen to titanium ratio for each particle is calculated according to Eq. 4. The solid state oxidation of particles is assumed here to be insignificant due to the low concentration of O_2 (see Fig. 4(b)).

Figure 11 shows the particle frequency map with respect to σ_O and primary particle size for growth parameter set 2. For all flames, σ_O is within 1.75–1.85. In each flame, small particles are shown to have a broader distribution of oxygen deficiency compared to the larger particles. The convergence of σ_O for large particles is due to the averaging effect as particles grow through coalescence. This suggests that σ_O is very sensitive to the very early stages of particle formation.

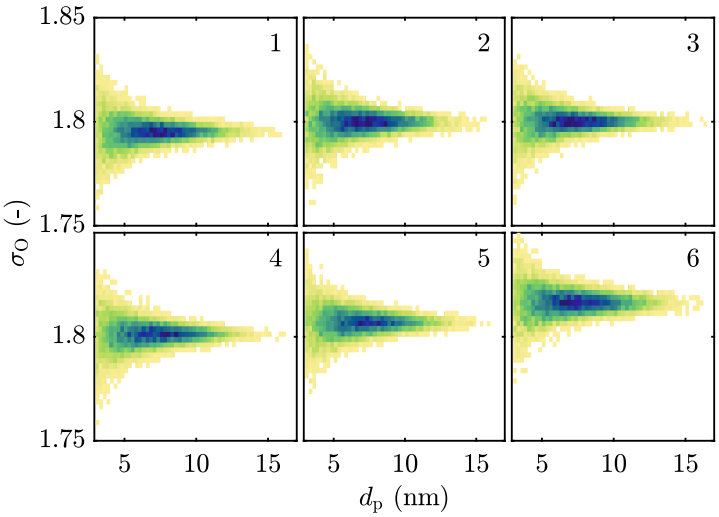

Figure 11: *The 2D frequency map with respect to particle size (d_p) and oxygen to titanium ratio (σ_O) for particles at stagnation point using growth parameter set 2 (Table 2) for flames 1–6. The color represents the frequency (blue: highest, yellow: lowest).*

The average oxygen to titanium ratio in the particle population as a function of the flame dilution is shown in **Fig. 12**. The average σ_O is insensitive to the temperature which corresponds to the particle residence time. This suggests that particle composition is determined very early in the formation stages (near the flame front) and no significant

changes occur in the cooling region. However, the average σ_O is strongly influenced by the choice of the growth parameters (see Table 2).

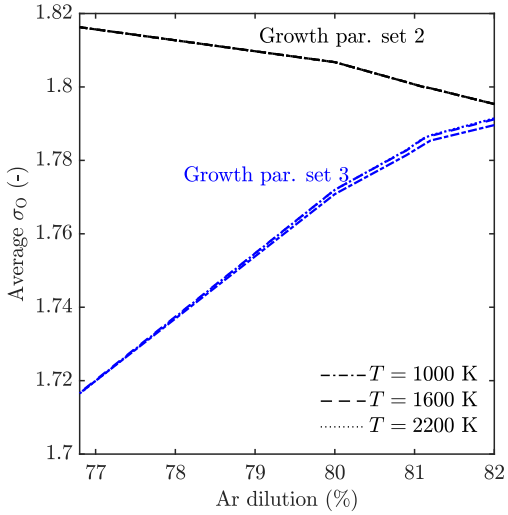

Figure 12: *The average particle oxygen to titanium ratio, σ_O, as a function of flame dilution at different temperature for growth parameter sets 2 and 3. The temperature here refers to the flame temperature in the cooling region (between the maximum temperature and the stagnation plate). For description of growth parameter sets, see Table 2.*

The contrasting predictions of models with growth parameter sets 2 and 3 can be explained as follows. As shown in Fig. 10, the shift of relative abundance of $Ti(OH)_3$ compared to $Ti(OH)_4$ occurs only in the post-flame region. This is a consequence of $Ti(OH)_4$ being formed first although $Ti(OH)_3$ is more stable than $Ti(OH)_4$. As the particle formation rate increases with temperature (due to the increase in collision rate), particle formation in hotter flames (lower Ar dilution) occurs earlier compared to the colder flames (higher Ar dilution). When the particle formation occurs earlier, less oxygen deficient particles form (due to higher amount of $Ti(OH)_4$ than $Ti(OH)_3$). As a result, σ_O decreases with increasing flame dilution for the growth parameter set 2 (fast inception and surface growth).

On the other hand, the opposite trend is expected when slower inception and surface growth rates are applied (growth parameter set 3). This results in particle formation occurring later where $Ti(OH)_3$ has had time to form. As the $Ti(OH)_3$ stability over $Ti(OH)_4$ increases with temperature, this leads to more $Ti(OH)_3$ formed in hotter flames (lower Ar dilution), leading to more oxygen deficient particles (smaller σ_O). Therefore, σ_O increases with flame dilution as shown in Fig. 12. Growth parameter set 3 thus represents a case where the particle composition is controlled mainly by thermodynamics (closer to equilibrium) while the kinetic effect is more dominant in case growth parameter set 2.

It is important to note that σ_O is strongly influenced by the actual rates of inception and surface growth which are unknown. Thus the absolute values σ_O in Fig. 10 are unlikely to represent the actual particle composition. However, the trends in Fig. 10 are important because they reflect the impact of the temperature on the stability of small Ti-species, in particular $Ti(OH)_3$ and $Ti(OH)_4$ and their subsequent interaction with incipient Ti-O

clusters.

Composition model

From the experimental data in Fig. 2, anatase stability relative to rutile increases with increasing flame dilution. Based on the composition-dependent hypothesis, the increasing anatase stability is a result of a smaller of oxygen deficiencies in more diluted flames (larger σ_O). Thus, σ_O has to increase as a function of the flame dilution. As shown in Fig. 10, this is only true when particle formation is relatively slow (growth parameter set 3).

Here a composition-based model is proposed in which the anatase-rutile crossover size is dependent on the particle composition to explain the experimental data assuming the growth parameter set 3 (Table 2). Based on the comparison between the Gibbs energy and the melting models, it was shown that a size-dependent transformation temperature is not very important in this case. This is because the particles have very narrow size distributions. Thus, the transformation temperature is imposed here as a constant similar to the Gibbs energy model. Next, the crossover size d_{cross} is assumed to be a function of $\sigma_{O,i}$. These can be written as follows,

$$T_{\text{trans},i} = \lambda_1 \tag{26}$$

$$d_{\text{cross},i} = F(\sigma_{O,i}) \tag{27}$$

The explicit form of F is not known. Based on the composition-dependent hypothesis, the crossover size should increase with increasing σ_O, approaching the value predicted by thermodynamic analysis for stoichiometric composition ($\sigma_O = 2$). Here, F is approximated by a surrogate function $G(x)$ that fulfills the following conditions: (1) $G(x)$ is positive for $x > 0$, and (2) $G(x)$ increases with increasing x, i.e. $\mathrm{d}G/\mathrm{d}x > 0$. An error function based G is here used as the surrogate function,

$$F(x) \approx G(x) = \lambda_2 + \lambda_3 \mathrm{erf}[\lambda_4(x - \lambda_5)] \quad \lambda_2, \lambda_3, \lambda_4, \lambda_5 \geq 0, \tag{28}$$

where λ_2, λ_3, λ_4, and λ_5 are the free parameters of the composition model.

The rutile fraction function in Eq. 9 for growth parameter set 3 is now written as

$$\mathrm{f_R} = f_{\text{comp}}(y; z^{(3)}, \theta) \quad \text{where } \theta = [\lambda_1, \lambda_2, \lambda_3, \lambda_4, \lambda_5]. \tag{29}$$

The best fit parameters $\hat{\theta}_3 = [2000\ \text{K}, 9.1\ \text{nm}, 3.9\ \text{nm}, 120, 1.79]$ (using growth parameter set 3, i.e. $z^{(3)}$) is evaluated according to Eq. 10. The transformation temperature is 2000 K and the function $G(\sigma_O)$ is given as

$$G(\sigma_O) = 9.1 + 3.8\mathrm{erf}[120(\sigma_O - 1.79)] \ \ (\text{nm}), \tag{30}$$

which is shown in **Fig. 13(a)**. The function G has a sharp transition at $\sigma_O = 1.79$. However, as discussed above the absolute values of σ_O predicted in this model are strongly dependent on the model assumptions. Thus, the precise location of the transition in function G, σ_O^*, is uncertain. The physical mechanism responsible for this sharp transition is

unclear and requires further investigation. One possible interpretation is that below a certain oxygen deficiency ($\sigma_O < \sigma_O^*$), one of the sub-oxides in the Magnéli series is formed [2]. These sub-oxides are line compounds in TiO_2 phase diagram and therefore only formed at specific compositions [35]. These sub-oxides are hypothesised to favour rutile formation due to the similarity between their crystal structures and rutile's and therefore results in a decrease in the anatase-rutile crossover size. At larger σ_O, the crossover size or G in Fig. 13(a) approaches 13 nm which is very close to the value calculated by [53] (14 nm).

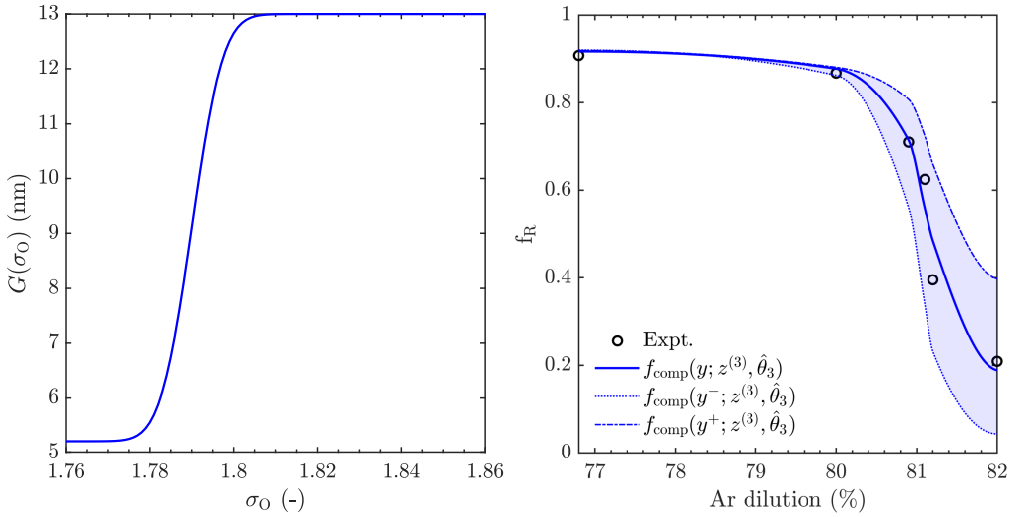

Figure 13: *(a) The function G describing the crossover size dependency on σ_O (Eq. 30) from the parameter estimation. (b) The measured and predicted rutile fractions as a function of Ar dilution for growth parameter set 3 (i.e. $z^{(3)}$) using the fitted parameter $\hat{\theta}_3$. Also shown are the rutile fractions assuming mixture equivalence ratio of 0.99 (y^-) and 1.01 (y^+) to indicate the uncertainty from the experimental flowrates.*

Figure 13(b) shows the simulated rutile fractions with the best fitted parameters for the growth parameter set 3. The model shows an excellent agreement with the experimental data. In addition, the predicted rutile fractions for mixtures with equivalence ration of 0.99 and 1.01 (assuming the same Ar dilution in Table 1) are shown. These represents the uncertainty (shaded area) due to the fluctuation in the experimental flowrates. This suggests that the model is highly sensitive to the equivalence ratio, especially at higher Ar dilution, which may explain the narrow range of equivalence ratio in which anatase-rutile stability sensitivity has been reported before [21, 30].

The varying composition of the incipient particles implied in the composition model proposed here can potentially explain the formation of the metastable phases reported here and in other studies [30, 40]. It was suggested that oxygen deficient cluster intermediates are responsibe for the formation of TiO_2-II which is not predicted by the thermodynamic stability analysis [30]. In particular, Ti_3O_5 has been shown to be a potential intermediate for TiO_2-II due to the small mismatch between the α-Ti_3O_5 and TiO_2-II structures [17]. TiO_2-B phase was shown to form during the dehydration of titanic acids $Ti_4O_7(OH)_2(H_2O)_n$ [47]. These titanic acids can be seen as hydroxylated TiO_2 chains

which are likely to form in oxygen rich conditions. In addition TiO_2-B eventually transforms into anatase due to the topotactic relationship between their structures [7] which explains the formation of TiO_2-B/anatase mixure in oxygen rich conditions [30].

While the model proposed here shows an excellent agreement with the experiments, a number of simplifying assumptions are made including the clustering mechanism, particle precursors, and reaction rates. This analysis highlights the need for a better chemical model that describes the early stage formation of particles for predicting the phase composition despite its apparent small impact on the particle size or morphology. For example, Ershov et al. [13] recently suggested that the TTIP decomposition mechanism proposed by [9] is missing an important pathway, i.e. the acetone abstraction pathway. This is especially important in this case as the acetone abstraction reaction results in fewer oxidised species (with lower oxidation state of Ti) forming earlier, which then gradually oxidise in the flame. This would significantly affect the particle precursor concentration and in turn the composition of the incipient particles.

Further, some potentially important effects are not yet captured in the model discussed in this work. For example, the formation of the metastable phases suggests that the kinetic aspects of the phase transformation need to be considered. The effect of the oxygen defficiency on the transition temperature between non-crystalline and crystalline phases may also be important. Knaup et al. [22], using molecular dynamics simulations, show that the oxygen defficiency induces a significant reduction in the melting temperature of rutile. These effects will be investigated in a future work.

5 Conclusions

In this paper, new experimental measurements of TiO_2 phase composition as a function of the flame dilution for stoichiometric mixtures are reported. The measurements demonstrated a high sensitivity of the anatase-rutile stability as a function of the flame dilution. Anatase is shown to form at higher flame dilution while rutile is favoured at lower flame dilution. The results are surprising as the oxygen content of the initial mixture decreases with increasing flame dilution which is expected to favour rutile formation.

The effect of the flame dilution on the relative anatase-rutile composition is investigated by comparing experimental data and model predictions based on different assumptions on two particle formation pathways/mechanisms. The phase transformation model is assumed to be controlled by a crossover size. The analysis in this paper seeks to answer the question of whether the sensitivity observed in the experimental measurements can be explained by a surface energy-dependent model (first mechanism) or particle composition model (second mechanism).

In the first mechanism, a stoichiometric TiO_2 intermediate is assumed and the anatase-rutile crossover size is controlled mainly by the surface energy. The dependency of the crossover size on surface energy can be represented by two different models (Gibbs energy and melting models) that treat the particle polydispersity differently. These models predict a correct trend of anatase-rutile stability as a function of the flame dilution. However, they fail to reproduce the sensitivity observed in the experiments.

The second mechanism takes into account the possible formation of oxygen-deficient clusters that act as particle precursors. Given the assumptions made about the clustering mechanism, a composition-based model is proposed in which the crossover size is a function of the particle composition. The model shows an excellent agreement with the experimental data. In addition, the suboxide intermediates considered in this model provide a plausible explanation for the formation of metastable phases. However, it is demonstrated that the predicted anatase-rutile composition strongly depends on the assumptions made about the initial stages of particle formation, which are currently little understood. This highlights the importance of developing a better chemical mechanism in order to understand the phase formation mechanism.

Acknowledgements

This project is supported by the National Research Foundation (NRF), Prime Minister's Office, Singapore under its Campus for Research Excellence and Technological Enterprise (CREATE) programme. The authors thank Venator and CMCL Innovations for generous financial support. Markus Kraft acknowledges the support of the Alexander von Humboldt foundation.

A Particle processes

In this work, $Ti(OH)_3$ and $Ti(OH)_4$ are treated as the gas-phase collision species for particle inception and surface growth. This section describes the particle composition transformations in the detailed particle model under these processes. The process rates and geometric transformations are described in [26].

A.1 Inception

A particle containing a single primary, assumed to be in the non-crystalline (NC) phase, is incepted from a bimolecular collision of gas-phase species. The three possible collisions are:

$$\begin{aligned} &2\,Ti(OH)_4 \rightarrow 4\,H_2O \\ &\quad + P_q\left(p_1\left(\eta_{Ti,NC}=2, \eta_{O,NC}=4, \eta_{Ti,An}=0, \eta_{O,An}=0, \eta_{Ti,Ru}=0, \eta_{O,Ru}=0, r, \mathbf{x}\right), \mathbf{C}\right). \end{aligned} \tag{A.1}$$

$$\begin{aligned} &2\,Ti(OH)_3 \rightarrow 3\,H_2O \\ &\quad + P_q\left(p_1\left(\eta_{Ti,NC}=2, \eta_{O,NC}=3, \eta_{Ti,An}=0, \eta_{O,An}=0, \eta_{Ti,Ru}=0, \eta_{O,Ru}=0, r, \mathbf{x}\right), \mathbf{C}\right). \end{aligned} \tag{A.2}$$

$$\begin{aligned} &Ti(OH)_4 + Ti(OH)_3 \rightarrow 3.5\,H_2O \\ &+ P_q\left(p_1\left(\eta_{Ti,NC}=2, \eta_{O,NC}=3.5, \eta_{Ti,An}=0, \eta_{O,An}=0, \eta_{Ti,Ru}=0, \eta_{O,Ru}=0, r, \mathbf{x}\right), \mathbf{C}\right). \end{aligned} \tag{A.3}$$

A.2 Surface growth

Surface growth is treated as a collision between a gas-phase species and a particle. As per Lindberg et al. [26], the mass is added to a primary p_i selected with probability proportional to its surface area relative to that of the entire aggregate particle. The number of Ti and O atoms of phase θ in the selected primary is increased. The phase θ is chosen with probability proportional to the relative phase composition of the primary. Two collisions are defined:

$$P_q + Ti(OH)_4 \rightarrow P_q\left(\ldots, p_i\left(\eta_{Ti,\theta}+1, \eta_{O,\theta}+2, \ldots, r+\Delta r, \mathbf{x}\right), \ldots, \mathbf{C}\right) + 2H_2O. \tag{A.4}$$

$$P_q + Ti(OH)_3 \rightarrow P_q\left(\ldots, p_i\left(\eta_{Ti,\theta}+1, \eta_{O,\theta}+1.5, \ldots, r+\Delta r, \mathbf{x}\right), \ldots, \mathbf{C}\right) + 1.5H_2O. \tag{A.5}$$

A.3 Model parameters

Table 3: *Summary of particle model parameters.*

Parameter	Value
Collision limited processes:	
Enhancement factor, ε	2.64
Inception efficiency, γ_{IN}	see Table 2
Surface growth efficiency, γ_{SG}	see Table 2
Sintering:	
Prefactor, A_s	0.25
Critical diameter, $d_{p,crit}$	4 nm
Critical exponent, α_{crit}	3
Other:	
Density, ρ	3.84 g/cm^3

B Sensitivity analysis

A sensitivity function S_m is defined as

$$S_m(\theta) = \frac{1}{N_{\text{exp}}(N_{\text{exp}}-1)} \sum_{j=1}^{N_{\text{exp}}} \sum_{k\neq j}^{N_{\text{exp}}} \frac{f(x^{(j)};z^{(m)},\theta) - f(x^{(k)};z^{(m)},\theta)}{\mathrm{f}_{\mathrm{R}}^{\text{exp},(j)} - \mathrm{f}_{\mathrm{R}}^{\text{exp},(k)}}, \tag{B.1}$$

where N_{exp} is the number of experimental conditions which is 6 in this case, f is the rutile fraction function of the model, $x^{(j)}$ is a vector of process conditons for flame j, $z^{(m)}$ is a vector of growth parameter set m (described in Table 2), θ is a vector of phase transformation parameters (defined for each model in Eqs. 16 and 23), $\mathrm{f}_{\mathrm{R}}^{\text{exp},j}$ is the rutile fraction from the experimental measurement for flame j.

The sensitivity function describes the sensitivity of rutile fraction to the flame conditions relative to the experimental data. Therefore, $S = 1$ represents a good agreement between the model and the measurements. The sensitivities for the Gibbs energy model and the melting model are shown in **Figs. 14 and 15**. The plots suggest that the models predict much lower sensitivity ($\sim$30% of the measured sensitivity) within the parameter space considered. In addition, the sensitivities are similar for the different growth parameter sets used. This suggests that the rutile fractions predicted by these models are insensitive to the assumptions on the initial particle growth stages.

The highest sensitivities are observed for transformation temperature of 1900–2000 K (α_2 and T^*) and crossover size of 6–10 nm (α_1 and d^*) in Figs. 14 and 15. These approximately coincide with the best fit parameters for these two models (see main text), i.e. $\hat{\theta} = [7\ \text{nm}, 2000\ \text{K}]$. It is noted that an upper limit of 2000 K is assumed for the transformation temperature as the bulk anatase has a melting point of 2075 K.

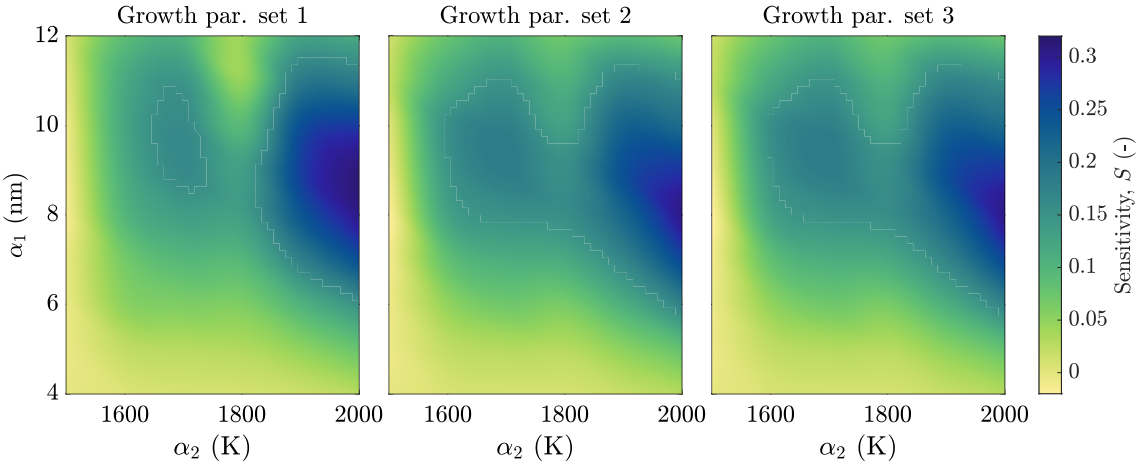

Figure 14: *The sensitivity function evaluated according to Eq. B.1 for Gibbs energy model, $f_{\text{Gibbs}}(y;z^{(m)},\theta)$, $\theta = [\alpha_1, \alpha_2]$ with growth parameter sets 1 ($m = 1$, left), 2 ($m = 2$, right), and 3 ($m = 3$, right). For description of growth parameter sets, see Table 2.*

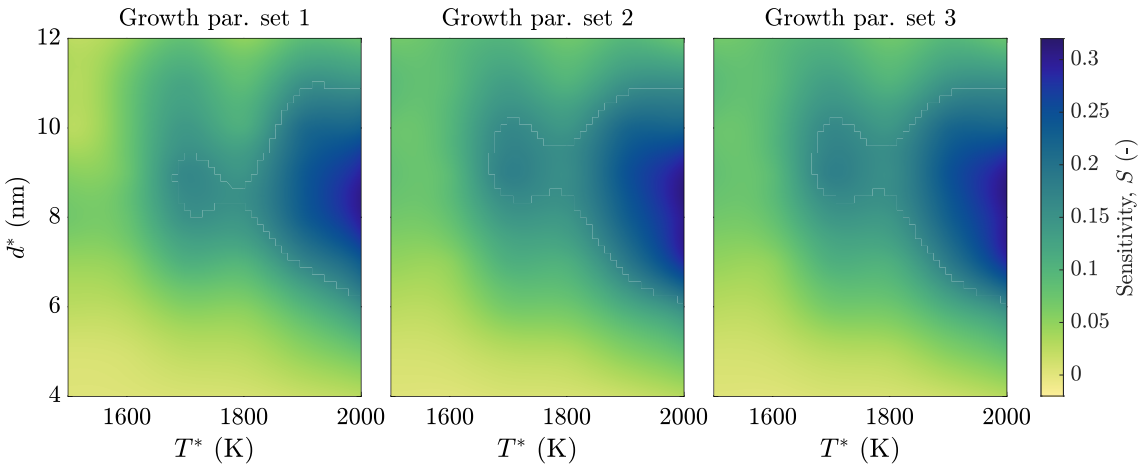

Figure 15: *The sensitivity function evaluated according to Eq. B.1 for melting model,* $f^*_{\text{melt}}(y; z^{(m)}, \theta^*)$, $\theta^* = [d^*, T^*]$ *with growth parameter sets 1 (*$m = 1$*, left), 2 (*$m = 2$*, right), and 3 (*$m = 3$*, right). For description of growth parameter sets, see Table 2.*

C Effect of equivalence ratio

Using equilibrium calculations as a proxy, the correlation between the ratio of $Ti(OH)_3$ to $Ti(OH)_4$ and anatase-rutile stability can be applied to explain the effect of mixture equivalence ratio (ϕ). **Figure 16** shows the ratio of $Ti(OH)_3$ to $Ti(OH)_4$ from equilibrium calculations for mixtures corresponding to the flames with varying equivalence ratio reported previously [30]. The trend shown in Fig 16 is consistent with composition-dependent hypothesis as lean flames ($\phi < 1$) were shown to favour anatase while rich flames ($\phi > 1$) favour rutile formation.

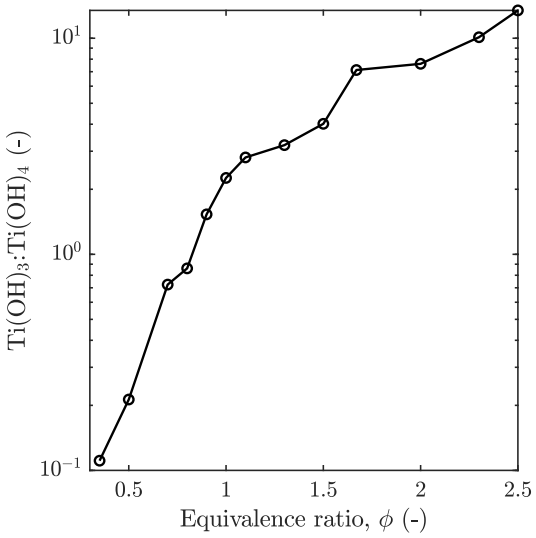

Figure 16: *Ratio of $Ti(OH)_3$ to $Ti(OH)_4$ mole fractions from equilibrium calculations as a function of mixture equivalence ratio. The mixture equivalence ratios shown here correspond to the flames reported in ref [30].*

References

[1] K. M. Akhtar, S. E. Pratsinis, and S. V. R. Mastrangelo. Vapor phase synthesis of Al-doped titania powders. *J. Mater. Res.*, 9(5):1241–1249, 1994. doi:10.1557/JMR.1994.1241.

[2] S. Andersson, B. Collén, U. Kuylenstierna, and A. Magnéli. Phase analysis studies on the titanium-oxygen system. *Acta Chem. Scand.*, 11:1641–1652, 1957. doi:10.3891/acta.chem.scand.11-1641.

[3] A. S. Barnard and H. Xu. An environmentally sensitive phase map of titania nanocrystals. *ACS Nano*, 2(11):2237–2242, 2008. doi:10.1021/nn800446w.

[4] A. S. Barnard and P. Zapol. Effects of particle morphology and surface hydrogenation on the phase stability of TiO_2. *Phys. Rev. B*, 70(23):1–13, 2004. doi:10.1103/PhysRevB.70.235403.

[5] J. Birkenstock, R. X. Fischer, and T. Messner. BRASS, the Bremen Rietveld analysis and structure suite. *Zeitschrift für Krist.*, 23:237–242, 2006.

[6] A. Bouzoubaa, A. Markovits, M. Calatayud, and C. Minot. Comparison of the reduction of metal oxide surfaces: TiO_2-anatase, TiO_2-rutile and SnO_2-rutile. *Surf. Sci.*, 583(1):107–117, 2005. doi:10.1016/j.susc.2005.03.029.

[7] L. Brohan, A. Verbaere, M. Tournoux, and G. Demazeau. La transformation TiO_2(B) $\rightarrow$ anatase. *Mater. Res. Bull.*, 17(3):355–361, 1982. doi:10.1016/0025-5408(82)90085-X.

[8] P. Buerger, D. Nurkowski, J. Akroyd, S. Mosbach, and M. Kraft. First-principles thermochemistry for the thermal decomposition of titanium tetraisopropoxide. *J. Phys. Chem. A*, 119(30):8376–8387, 2015. doi:10.1021/acs.jpca.5b01721.

[9] P. Buerger, D. Nurkowski, J. Akroyd, and M. Kraft. A kinetic mechanism for the thermal decomposition of titanium tetraisopropoxide. *Proc. Combust. Inst.*, 36(1): 1019–1027, 2017. doi:10.1016/j.proci.2016.08.062.

[10] CMCL Innovations. *k*inetics®, 2019. URL `http://www.cmclinnovations.com/`.

[11] N. A. Deskins, J. Du, and P. Rao. The structural and electronic properties of reduced amorphous titania. *Phys. Chem. Chem. Phys.*, 19(28):18671–18684, 2017. doi:10.1039/c7cp02940c.

[12] U. Diebold. The surface science of titanium dioxide. *Surf. Sci. Rep.*, 48:53–229, 2003. doi:10.1016/S0167-5729(02)00100-0.

[13] K. S. Ershov, S. A. Kochubei, V. G. Kiselev, and A. V. Baklanov. Decomposition pathways of titanium isopropoxide $Ti(OiPr)_4$: New insights from UV-photodissociation experiments and quantum chemical calculations. *J. Phys. Chem. A*, 122(4):1064–1070, 2018. doi:10.1021/acs.jpca.7b10396.

[14] J. Fang, Y. Wang, J. Kangasluoma, M. Attoui, H. Junninen, M. Kulmala, T. Petäjä, and P. Biswas. Cluster formation mechanisms of titanium dioxide during combustion synthesis: Observation with an APi TOF. *Aerosol Sci. Technol.*, 51(9):1071–1081, 2017. doi:10.1080/02786826.2017.1331028.

[15] M. Goodson and M. Kraft. An efficienct stochastic algorithm for simulating nano-particle dynamics. *J. Comput. Phys.*, 183(1):210–232, 2002. doi:10.1006/jcph.2002.7192.

[16] F. A. Grant. Properties of rutile (titanium dioxide). *Rev. Mod. Phys.*, 31(3):646—-674, 1959. doi:10.1103/RevModPhys.31.646.

[17] I. E. Grey, C. Li, I. C. Madsen, and G. Braunshausen. TiO_2-II. Ambient pressure preparation and structure refinement. *Mater. Res. Bull.*, 23:743–753, 1988. doi:10.1016/0025-5408(88)90040-2.

[18] G. Guisbiers, O. Van Overschelde, and M. Wautelet. Theoretical investigation of size and shape effects on the melting temperature and energy bandgap of TiO_2 nanostructures. *Appl. Phys. Lett.*, 92(10), 2008. doi:10.1063/1.2897297.

[19] S. Ishizuka, Y. Kimura, and T. Yamazaki. In situ FT-IR study on the homogeneous nucleation of nanoparticles of titanium oxides from highly supersaturated vapor. *J. Cryst. Growth*, 450:168–173, 2016. doi:10.1016/j.jcrysgro.2016.06.036.

[20] R. Jullien. Transparency effects in cluster-cluster aggregation with linear trajectories. *J. Phys. A*, 17:L771–L776, 1984.

[21] Y. K. Kho, W. Y. Teoh, L. Mädler, and R. Amal. Dopant-free, polymorphic design of TiO_2 nanocrystals by flame aerosol synthesis. *Chem. Eng. Sci.*, 66(11):2409–2416, 2011. doi:10.1016/j.ces.2011.02.058.

[22] J. M. Knaup, J. Marx, and T. Frauenheim. Reduction of the TiO_{2-x} melting temperature induced by oxygen deficiency with implications on experimental data accuracy and structural transition processes. *Phys. Status Solidi - Rapid Res. Lett.*, 8(6):549–553, 2014. doi:10.1002/pssr.201409042.

[23] L. Liborio and N. Harrison. Thermodynamics of oxygen defective Magnéli phases in rutile: A first-principles study. *Phys. Rev. B - Condens. Matter Mater. Phys.*, 77 (10):1–10, 2008. doi:10.1103/PhysRevB.77.104104.

[24] C. S. Lindberg, M. Y. Manuputty, J. Akroyd, and M. Kraft. A two-step simulation methodology for modelling stagnation flame synthesised aggregate nanoparticles. *Combust. Flame*, 202(204):143–153, 2019. doi:10.1016/j.combustflame.2019.01.010.

[25] C. S. Lindberg, M. Y. Manuputty, P. Buerger, J. Akroyd, and M. Kraft. Numerical simulation and parametric sensitivity study of titanium dioxide particles synthesised in a stagnation flame. *J. Aerosol Sci.*, (Submitted), 2019.

[26] C. S. Lindberg, M. Y. Manuputty, E. K. Y. Yapp, J. Akroyd, R. Xu, and M. Kraft. A detailed particle model for polydisperse titanium dioxide aggregates. *J. Comput. Phys.*, 397:108799, 2019. doi:10.1016/j.jcp.2019.06.074.

[27] C. Liu, J. Camacho, and H. Wang. Phase equilibrium of TiO_2 nanocrystals in flame-assisted chemical vapor deposition. *ChemPhysChem*, 19(2):180–186, 2018. doi:10.1002/cphc.201700962.

[28] H. K. Ma and H.-A. Yang. Combustion synthesis of titania nanoparticles in a premixed methane flame. *J. Alloys Compd.*, 504(1):115–122, 2010. doi:10.1016/j.jallcom.2010.05.066.

[29] M. Y. Manuputty, J. Akroyd, S. Mosbach, and M. Kraft. Modelling TiO_2 formation in a stagnation flame using method of moments with interpolative closure. *Combust. Flame*, 178:135–147, 2017. doi:10.1016/j.combustflame.2017.01.005.

[30] M. Y. Manuputty, J. A. H. Dreyer, Y. Sheng, E. J. Bringley, M. L. Botero, J. Akroyd, and M. Kraft. Polymorphism of nanocrystalline TiO_2 prepared in a stagnation flame: formation of the TiO_2-II phase. *Chem. Sci.*, 10:1342–1350, 2019. doi:10.1039/C8SC02969E.

[31] M. Y. Manuputty, C. S. Lindberg, M. L. Botero, J. Akroyd, and M. Kraft. Detailed characterisation of TiO_2 nano-aggregate morphology using TEM image analysis. *J. Aerosol Sci.*, 133:96–112, 2019. doi:10.1016/j.jaerosci.2019.04.012.

[32] S. Memarzadeh, E. D. Tolmachoff, D. J. Phares, and H. Wang. Properties of nanocrystalline TiO_2 synthesized in premixed flames stabilized on a rotating surface. *Proc. Combust. Inst.*, 33(2):1917–1924, 2011. doi:10.1016/j.proci.2010.05.065.

[33] P. K. Naicker, P. T. Cummings, H. Zhang, and J. F. Banfield. Characterization of titanium dioxide nanoparticles using molecular dynamics simulations. *J. Phys. Chem. B*, 109(32):15243–15249, 2005. doi:10.1021/jp050963q.

[34] J. Nowotny, T. Bak, M. K. Nowotny, and L. R. Sheppard. Defect chemistry and electrical properties of titanium dioxide. 1. Defect diagrams. *J. Phys. Chem. C*, 112 (2):602–610, 2008. doi:10.1021/jp0745642.

[35] H. Okamoto. O-Ti (Oxygen-Titanium). *J. Phase Equilibria*, 22(4):515–515, 2003. doi:10.1361/105497101770338635.

[36] P. M. Oliver, G. W. Watson, E. T. Kelsey, and S. C. Parker. Atomistic simulation of the surface structure of the TiO_2 polymorphs rutile and anatase. *J. Mater. Chem.*, 7 (3):563–568, 1997. doi:10.1039/a606353e.

[37] R. I. Patterson, J. Singh, M. Balthasar, M. Kraft, and W. Wagner. Extending stochastic soot simulation to higher pressures. *Combust. Flame*, 145(3):638–642, 2006. doi:10.1016/j.combustflame.2006.02.005.

[38] R. I. A. Patterson, J. Singh, M. Balthasar, M. Kraft, J. R. Norris, and M. Carlo. The linear process deferment algorithm: A new technique for solving population balance equations. *SIAM J. Sci. Comput.*, 28(1):303–320, 2006. doi:10.1137/040618953.

[39] M. R. Ranade, A. Navrotsky, H. Z. Zhang, J. F. Banfield, S. H. Elder, A. Zaban, P. H. Borse, S. K. Kulkarni, G. S. Doran, and H. J. Whitfield. Energetics of nanocrystalline TiO_2. *Proc. Natl. Acad. Sci.*, 99(Supplement 2):6476–6481, 2002. doi:10.1073/pnas.251534898.

[40] K. B. Riad, P. M. Wood-adams, and K. Wegner. Flame-made TiO_2(B). *Mater. Res. Bull.*, 106(June):276–281, 2018. doi:10.1016/j.materresbull.2018.06.017.

[41] S. Shekar, W. J. Menz, A. J. Smith, M. Kraft, and W. Wagner. On a multivariate population balance model to describe the structure and composition of silica nanoparticles. *Comput. Chem. Eng.*, 43:130–147, 2012. doi:10.1016/j.compchemeng.2012.04.010.

[42] A. G. Shmakov, O. P. Korobeinichev, D. A. Knyazkov, A. A. Paletsky, R. A. Maksyutov, I. E. Gerasimov, T. A. Bolshova, V. G. Kiselev, and N. P. Gritsan. Combustion chemistry of $Ti(OC_3H_7)_4$ in premixed flat burner-stabilized H_2/O_2/Ar flame at 1 atm. *Proc. Combust. Inst.*, 34(1):1143–1149, 2013. doi:10.1016/j.proci.2012.05.081.

[43] R. A. Spurr and H. Myers. Quantitative analysis of anatase-rutile mixtures with an x-ray diffractometer. *Anal. Chem.*, 29(5):760–762, 1957. doi:10.1021/ac60125a006.

[44] A. Teleki and S. E. Pratsinis. Blue nano titania made in diffusion flame. *Phys. Chem. Chem. Phys.*, 11(19):3742–3747, 2009. doi:10.1039/b905768d.

[45] E. D. Tolmachoff, A. D. Abid, D. J. Phares, C. S. Campbell, and H. Wang. Synthesis of nano-phase TiO_2 crystalline films over premixed stagnation flames. *Proc. Combust. Inst.*, 32(2):1839–1845, 2009. doi:10.1016/j.proci.2008.06.052.

[46] E. D. Tolmachoff, S. Memarzadeh, and H. Wang. Nanoporous titania gas sensing films prepared in a premixed stagnation flame. *J. Phys. Chem. C*, 115(44):21620–21628, 2011. doi:10.1021/jp206061h.

[47] M. Tournoux, R. Marchand, and L. Brohan. Layered $K_2Ti_4O_9$ and the open metastable TiO_2(B) structure. *Prog. Solid State Chem.*, 17:33–52, 1986. doi:10.1016/0079-6786(86)90003-8.

[48] S. Vemury and S. E. Pratsinis. Dopants in flame synthesis of titania. *J. Am. Ceram. Soc.*, 78(11):2984–92, 1995. doi:10.1111/j.1151-2916.1995.tb09074.x.

[49] H. Wang, X. You, A. V. Joshi, S. G. Davis, A. Laskin, F. N. Egolfopoulos, and C. K. Law. USC mech version II: High-temperature combustion reaction model of H_2/CO/C_1-C_4 compounds, 2007. URL `http://ignis.usc.edu/USC_Mech_II.htm`.

[50] Y. Wang, J. Kangasluoma, M. Attoui, J. Fang, H. Junninen, M. Kulmala, T. Petäjä, and P. Biswas. Observation of incipient particle formation during flame synthesis by tandem differential mobility analysis-mass spectrometry (DMA-MS). *Proc. Combust. Inst.*, 36(1):745–752, 2017. doi:10.1016/j.proci.2016.07.005.

[51] S. Wu, W. Wang, W. Tu, S. Yin, Y. Sheng, M. Y. Manuputty, M. Kraft, and R. Xu. Premixed stagnation flame synthesized TiO_2 nanoparticles with mixed phases for efficient photocatalytic hydrogen generation. *ACS Sustain. Chem. Eng.*, 6(11):14470–14479, 2018. doi:10.1021/acssuschemeng.8b03142.

[52] J. Yang, Y. X. Huang, and J. M. F. Ferreira. Inhibitory effect of alumina additive on the titania phase transformation of a sol-gel-derived powder. *J. Mater. Sci. Lett.*, 16 (23):1933–1935, 1997. doi:10.1023/A:1018590701831.

[53] H. Zhang and J. F. Banfield. Thermodynamic analysis of phase stability of nanocrystalline titania. *J. Mater. Chem.*, 8(9):2073–2076, 1998. doi:10.1039/a802619j.

[54] H. Zhang and J. F. Banfield. Structural characteristics and mechanical and thermodynamic properties of nanocrystalline TiO_2. *Chem. Rev.*, 114(19):9613–9644, 2014. doi:10.1021/cr500072j.